Analysis of heat losses from the cabin of a battery electric vehicle

Master's thesis in Mobility Engineering - Automotive

RAUL ROYO BARENG

DEPARTMENT OF MECHANICS AND MARITIME SCIENCES

CHALMERS UNIVERSITY OF TECHNOLOGY
Gothenburg, Sweden 2023
www.chalmers.se

MASTER'S THESIS 2023

Analysis of heat losses from the cabin of a battery electric vehicle

RAUL ROYO BARENG

Department of Mechanics and Maritime Sciences
Division of Vehicle Engineering and Autonomous Systems
CHALMERS UNIVERSITY OF TECHNOLOGY
Gothenburg, Sweden 2023

Analysis of heat losses from the cabin of a battery electric vehicle

RAUL ROYO BARENG

Supervisor: Anandh Ramesh Babu
Examiner: Simone Sebben

Master's Thesis 2023
Department of Mechanics and Maritime Sciences
Division of Vehicle Engineering and Autonomous Systems
Chalmers University of Technology
SE-412 96 Gothenburg
Telephone +46 31 772 1000

Typeset in LaTeX
Printed by Chalmers Reproservice
Gothenburg, Sweden 2023

Analysis of heat losses from the cabin of a battery electric vehicle
RAUL ROYO BARENG
Department of Mechanics and Maritime Sciences
Division of Vehicle Engineering and Autonomous Systems
Chalmers University of Technology

Abstract

Thermal comfort and air quality are crucial for the efficient operation of Battery Electric Vehicles (BEVs). Unlike Internal Combustion Engine (ICE) vehicles, which use the engine waste heat energy in their heating and cooling systems, BEVs rely solely on electrical energy stored in traction batteries, making thermal management essential for their driving range. Achieving suitable thermal comfort and air quality in a BEV cabin has therefore a greater impact on driving range compared to ICE vehicles. This study aimed to understand heat transfer effects in a car cabin and their impact in energy-efficient climate control in BEVs.

Computer Fluid Dynamics (CFD) simulations were conducted to investigate heat transfer within a BEV cabin during a cool-down scenario. The study focused on a simplified geometry resembling the boundaries of an actual car cabin, considering factors such as the value of total air mass flow rate, conduction, convection, solar loads, air mass flow distribution, and driver presence.

Results showed that during a summer night drive (no solar loads) at 32 km/h and 43ºC ambient temperature, cooling the cabin with a total air mass flow rate of 68.5 g/s and 7ºC inlet air temperature lead to average air temperature variations of ±2ºC inside the cabin, considering different levels of insulation. On a summer day, considering moderate and intense solar loads, variations of ±5ºC on the average air temperature were observed. Applying the total air mass flow rate only at the top air inlets increased the average temperature by 1ºC but improved passengers' local temperature distribution. In order to achieve thermal comfort inside the car cabin, at least 120 g/s total air mass flow rate was required in an intense solar load scenario, whereas only 95 g/s was required in a moderate solar load scenario. At least 15 g/s total air mass flow was required to achieve proper ventilation of carbon dioxide in the presence of the driver. A time-step of 1 s was sufficient to capture the overall time evolution of temperature at probe points of interest.

The study concluded that achieving thermal comfort and proper air quality inside a simplified car cabin required careful consideration of the total air mass flow rate. The analysis of heat fluxes at cabin boundaries and the energy consumption of the HVAC unit further contributed to understanding the system. By gaining insights into heat transfer mechanisms and improving thermal management strategies, BEV manufacturers can enhance cabin comfort, air quality, and overall energy efficiency, ultimately maximizing the driving range of these vehicles.

Keywords: cabin, BEV, HVAC, CFD, airflow, heat transfer, solar loads.

Acknowledgements

The Computer Fluid Dynamics (CFD) simulations were conducted at the Vehicle Engineering and Autonomous Systems (VEAS) division at CHALMERS. I would like to thank my thesis supervisor Anandh Ramesh Babu and professor Simone Sebben for the warm welcome to the division, as well as for all the guidance, advice, and feedback I received during the progress of the research. I also want to mention and thank my family and friends, who supported and encouraged me to continue my education.

RAUL ROYO BARENG, Gothenburg, June 2023

List of Acronyms

Below is the list of acronyms that have been used throughout this thesis listed in alphabetical order:

BEV	Battery Electric Vehicle
CFD	Computer Fluid Dynamics
EU	European Union
HVAC	Heating, Ventilation and Air Conditioning
ICE	Internal Combustion Engine
LEV	Low-Emissions vehicle
PMV	Predicted Mean Vote
PPD	Predicted Percentage of Dissatisfied
RANS	Reynolds-Averaged Navier-Stokes
VOC	Volatile Organic Compound
ZEV	Zero-Emissions vehicle

Nomenclature

ρ: Density
Γ: Diffusion coefficient
S_ϕ: Source term for ϕ
∇p: Pressure gradient
k: Material thermal conductivity
h: Local heat transfer coefficient
$C_{\epsilon 1}$, $C_{\epsilon 2}$: Constants (k-ϵ model)
P: Production term (k-ϵ model)
β: Dissipation term (k-ϵ model)
σ_k, σ_ϵ: Constants (k-ϵ model)
$C_{\varepsilon 1}$, $C_{\varepsilon 2}$: Constants (realizable k-ϵ model)
S_k, S_ε: Source terms (realizable k-ϵ model)
constant
A, B: Constants
u_τ: Friction velocity
τ_w: Wall shear stress
Pr: Prandtl number
Pr_t: Turbulent Prandtl number
y^+: Dimensionless distance from the wall (viscous sublayer)
y^*: Dimensionless distance from the wall (thermal boundary layer)
t: Time
ϕ: Transport variable
$\mathbf{u}$: Velocity vector
CV: Integration Control Volume
$\mathbf{F}$: Vector field
A_{CV}: Surface area of the control volume
$\mathbf{n}$: Outward unit normal vector to the surface A_{CV}
Δt: Time interval
p: Pressure
$\boldsymbol{\tau}$: Stress tensor
$\mathbf{f}$: Body force vector
μ: Dynamic viscosity
$\mathbf{S_M}$: Source term for momentum
u: Velocity component in the x direction
v: Velocity component in the y direction
w: Velocity component in the z direction
S_x: Source term for the x momentum equation
S_y: Source term for the y momentum equation
S_z: Source term for the z momentum equation
$\mathbf{f}$: Gravitational force vector
E: Energy
$\mathbf{q}$: Heat flux vector
T: Temperature
T_∞: Characteristic temperature of the surroundings
H: Enthalpy
H_{static}: Static enthalpy
c_p: Specific heat at constant pressure
k: Turbulence kinetic energy
ϵ: Turbulence dissipation rate
μ_t: Turbulent viscosity
h: Heat transfer coefficient
Re: Reynolds number
Gr: Grashof number
Q_{rad}: Radiant heat transfer
q_{rad}: Radiant heat flux
σ: Stefan-Boltzmann constant
ϵ: Emissivity
α: Absortivity
τ: Transmitivity
ρ: Reflectivity
$q_{k,out}$: Radiant heat flux outgoing from surface k
$q_{k,in}$: Radiant heat flux incoming to surface k
ϵ_k: Emissivity of surface k
σ: Stefan-Boltzmann constant
F_{jk}: View factor from surface j to surface

k

n: Number of surfaces

θ_j: Angle between surface normal and incident radiation on surface j

θ_k: Angle between surface normal and incident radiation on surface k

r: Distance between surface j and surface k

dA: Differential area element

$q_{j,out}$: Radiant heat flux outgoing from surface j

$q_{k,in}$: Radiant heat flux incoming to surface k

τ_{xx}: Reynolds stress component in the x direction

τ_{yy}: Reynolds stress component in the y direction

τ_{zz}: Reynolds stress component in the z direction

τ_{xy}=τ_{yx}: Reynolds stress component between x and y directions

τ_{xz}=τ_{zx}: Reynolds stress component between x and z directions

τ_{yz}=τ_{zy}: Reynolds stress component between y and z directions

u': Turbulence fluctuation in the x direction

v': Turbulence fluctuation in the y direction

w': Turbulence fluctuation in the z direction

μ_t: Turbulent viscosity

U_i: Mean velocity component in the i direction

x_j: Spatial coordinate in the j direction

δ_{ij}: Kronecker delta

Contents

List of Figures

List of Tables

1

Introduction

The increase of efforts to replace the Internal Combustion Engine (ICE) vehicles for low and zero-emission vehicles, has led to the development of the Battery Electric Vehicles (BEV).

New ambitious targets are set by the European Union (EU) with regards to the electrification of cars in order to stop climate change. The national targets are stated in the EU Clean Vehicles Directive, which defines a clean vehicle as a low-emission vehicle (LEV) until 2025, and as a zero-emissions vehicle (ZEV) from 2026 onwards. Depending on the EU member state, minimum percentages within a range of 17.5% to 38.5% of the total new procured light-duty vehicles (cars and vans) must be clean vehicles.

As the demand for the BEV as a zero-emission vehicle increases, its of significant importance to improve its energy consumption, for instance designing an efficient interaction between the Heating, Ventilation, and Air Conditioning (HVAC) systems and the passengers cabin.

An important difference between ICE and BEV lies in the source of energy for their HVAC systems. While ICE vehicles use the waste of heat from the engine for heating purposes, BEVs totally rely on the energy stored in the traction battery. Efficient use of electrical energy is vital in BEVs to improve their driving range and maintain passenger comfort in terms of air quality and temperature.

In the context of BEV efficiency improvements, Computer Fluid Dynamics (CFD) simulations can be used as an important tool for the optimization in the design of the passengers cabin. These enable the virtual model and analysis of the airflow, temperature distribution, and heat transfer within the cabin. This approach can lead to the minimization of costs in design iterations, accelerating the development of the car cabin by providing a better understanding of the interaction with the HVAC units and heat transfer behaviors with the surroundings.

Simplified geometries in CFD simulations are used to find a balance between the calculation time and the accuracy of the obtained results. The main target of this thesis is to follow this approach, in order to study a methodology that could be applied within the automotive industry, which could lead to reliable results, which could speed up the design iterations. A cool-down scenario on a summer day is studied, in order to find the proper thermal comfort and air quality, as well as a reflection on the required power is presented.

The limitations of this project are that no specific model and test data are available and that the project is time constrained to 5 months.

2

Previous work

The study of thermal effects inside the cabin of vehicles has been a topic of research for the past years. CFD simulations have been widely carried out in different settings. Most of the studies are focused in determining the airflow patterns and air temperature inside the cabin in cool-down and warm-up scenarios [7,8,9,13,14]. Other research, performs the simulations by means of lumped models and no requirement for CFD analysis [6], or with a combination of software in addition to CFD [10]. In addition, models focused on the passengers' local thermal comfort have also been developed [2,10,11]. Optimization of thermal management strategies is also an interesting field of research [3]. Recently, the quality of air has also been considered by simulating the concentration of pollutants in the air [1,5]. Investigations on real cars regarding the actual measurement of total air mass flow rate and its distribution depending on the season have also been studied [12].

Among the literature regarding the thermal simulations by CFD, [7] validates CFD as a tool that can show good agreement with experimental data, and [9] corroborates that slight changes in the air direction at the inlets or the presence of a driver, substantially change the airflow patterns within the car cabin. Both studies conclude that thermal comfort within a car cabin can not be studied by standard models based on PMV-PPD [11], since the values of air velocity are high and variable. A comprehensive study on thermal comfort including passengers in CFD is provided by [2]. Nevertheless, these studies do not include the effect of solar loads, which have a significant effect on the overall temperature within a car cabin [8].

CFD studies [8,13,14] include solar loads. In [13], a corroboration of steady and transient simulations is made by comparison with real testing, using a simplified car cabin geometry. In [14], further research considers passengers in the cabin and concludes that thermal comfort depends on the number of passengers and recommends the improvement of insulation and glass transmissivity in order to reduce the cooling load. A deep study on the glass properties with regard to radiation can be found in [4]. In addition to solar loads, air quality plays an important role in the general comfort of the passengers. Source [1] offers interesting research on the carbon dioxide inside a car cabin depending on the number of passengers and the total air mass flow rate. Nevertheless, this research does not consider the effect of gravity nor the effect of solar loads. An interesting study regarding the presence of Volatile Organic Compounds (VOCs) is shown by [5], in which the emission of pollutants inside the cabin depends directly on the solar loads.

The target of the present research is to simulate all the heat transfer effects together with the presence of a driver, considering the air temperature and concentration of carbon dioxide. A reflection on the importance of thermal comfort, air quality, and its relation with power consumption, is made in the context of battery electric vehicles.

3

Theory

3.1 Governing equations

The transport of properties within a fluid domain can be modeled by a general equation. A general variable ϕ represents the properties of interest within the fluid, which can have the form of either a vector (e.g. velocity) or a scalar (e.g. temperature, enthalpy, internal energy, or pollutant concentration). The general transport equation is a partial differential equation (PDE) that describes the rate of change of the property in question to the transport mechanisms and external sources as a continuous problem [15].

$$\frac{\partial(\rho\phi)}{\partial t} + \nabla \cdot (\rho\phi\mathbf{u}) = \nabla \cdot (\Gamma\nabla\phi) + S_\phi \tag{3.1}$$

A discretization of this equation is required in order to numerically solve the problem of fluid properties transport for a domain of study by means of Computer Fluid Dynamics (CFD). This can be achieved by integrating the equation in three-dimensional control volumes (CV) within the domain of study. This approach is key to developing the Finite Volume Method (FVM).

$$\int_{CV} \frac{\partial(\rho\phi)}{\partial t} dV + \int_{CV} \nabla \cdot (\rho\phi\mathbf{u}) dV = \int_{CV} \nabla \cdot (\Gamma\nabla\phi) dV + \int_{CV} S_\phi dV \tag{3.2}$$

The transport mechanisms for ϕ are modeled as the divergence of vectorial fields related to convective and diffusive behaviors.

- Convection is the transport of ϕ in the fluid domain by mass flow $\rho\mathbf{u}$. The transport by convection is governed by the vectorial field defined by the fluid velocity $\mathbf{u}$.
- Diffusion is the transport of ϕ in the fluid domain by molecular processes Γ. The transport is governed by the vectorial field defined by the property gradient $\nabla\phi$.

It is necessary to apply Gauss's divergence theorem to relate the behavior of the property inside the control volumes to its behavior on the boundary of the control volumes. The theorem implies that the integral of the divergence of a vector field over a volume (CV for a control volume) is equal to the flux of the vector field through the closed surface around the mentioned volume (A_{CV} for a control volume).

$$\int_{CV} \nabla \cdot \mathbf{F} dV = \int_{A_{CV}} \mathbf{F} \cdot \mathbf{n} dA \tag{3.3}$$

Applying the theorem to the general transport equation integral over a control volume CV, the convective and diffusive transport of property ϕ can be treated as the integral of flux through the boundary A_{CV} of the control volume.

$$\frac{\partial}{\partial t}\int_{CV}(\rho\phi)dV + \int_{A_{CV}}(\rho\phi\mathbf{v})\cdot\mathbf{n}dA = \int_{A_{CV}}(\Gamma\nabla\phi)\cdot\mathbf{n}dA + \int_{CV}S_{\phi}dV \tag{3.4}$$

Analyzing the resulting integrated form of the general transport equation, the relationship can be expressed in words as the conservation of property ϕ for a fluid finite control volume.

At the left-hand side of the equation:

- Time term: it is the first term and it accounts for the rate of increase of ϕ in the control volume.
- Convective term: it is the second term and it accounts for the net rate of decrease of ϕ through the boundary of the control volume due to convection.

At the right-hand side of the equation:

- Diffusive term: it is the first term and it accounts for the net rate of increase of ϕ through the boundary of the control volume due to diffusion.
- Source term: it is the second term and it accounts for the rate of creation of ϕ in the control volume due to sources.

For steady-state problems, the rate of change of property ϕ is zero.

$$\int_{A_{CV}}(\rho\phi\mathbf{u})\cdot\mathbf{n}dA = \int_{A_{CV}}(\Gamma\nabla\phi)\cdot\mathbf{n}dA + \int_{CV}S_{\phi}dV \tag{3.5}$$

For unsteady problems, the time has to be integrated over an interval of time.

$$\int_{\Delta t}\frac{\partial}{\partial t}\int_{CV}(\rho\phi)dVdt + \int_{\Delta t}\int_{A_{CV}}(\rho\phi\mathbf{u})\cdot\mathbf{n}dAdt = \int_{\Delta t}\int_{A_{CV}}(\Gamma\nabla\phi)\cdot\mathbf{n}dAdt + \int_{\Delta t}\int_{CV}S_{\phi}dVdt \tag{3.6}$$

By setting the transport property variable ϕ to 1, velocity $\mathbf{u}$, enthalpy h, internal energy i, or temperature T, and choosing appropriate values for Γ and S_{ϕ}, the PDE and the integrated PDE forms can be obtained to define the continuity, momentum, and energy models within the fluid domain of study. This enables to numerically solve for the property variables by FVM discretization.

3.1.1 Continuty equation

The continuity PDE describes that the rate of increase of mass in a fluid element is equal to the net rate of flow of mass across the fluid element's boundaries. The rate of mass

$$\frac{\partial \rho}{\partial t} + \nabla \cdot (\rho \mathbf{u}) = 0 \tag{3.7}$$

With reference to the general transport equation, the continuity equation can be obtained if the general variable is assigned as $\phi = 1$.

3.1.2 Momentum equation

The momentum PDE describes that the rate of increase of momentum is equal to the sum of forces on a fluid particle (Newton's second law). The surface forces are compounded by pressure p normal force, viscous τ normal and tangential force, and gravitational $\mathbf{f} = \rho \mathbf{g}$ force.

$$\frac{\partial (\rho \mathbf{u})}{\partial t} + \nabla \cdot (\rho \mathbf{u}\mathbf{u}) = -\nabla p + \nabla \cdot \boldsymbol{\tau} + \mathbf{f} \tag{3.8}$$

Considering the fluid of study as a Newtonian fluid, the viscous stresses are proportional to the rates of deformation within the fluid. Additionally, if the fluid is considered incompressible (i.e. constant fluid density), the mass conservation equation is $\nabla \mathbf{v} = 0$, and thus the viscous stresses are twice the local rate of linear deformation times the dynamic viscosity μ. With these assumptions, the momentum equation can be represented in the Navier-Stokes form.

$$\frac{\partial (\rho \mathbf{u})}{\partial t} + \nabla \cdot (\rho \mathbf{u}\mathbf{u}) = -\nabla p + \nabla \cdot (\mu \nabla \mathbf{u}) + \mathbf{S_M} \tag{3.9}$$

Expanding the vectorial PDE, three equations are obtained for the components x, y and z.

$$\rho \frac{\partial u}{\partial t} + \rho u \frac{\partial u}{\partial x} + \rho v \frac{\partial u}{\partial y} + \rho w \frac{\partial u}{\partial z} = -\frac{\partial p}{\partial x} + \frac{\partial}{\partial x}(\mu \frac{\partial u}{\partial x}) + \frac{\partial}{\partial y}(\mu \frac{\partial u}{\partial y}) + \frac{\partial}{\partial z}(\frac{\partial u}{\partial z}) + S_x \tag{3.10}$$

$$\rho \frac{\partial v}{\partial t} + \rho u \frac{\partial v}{\partial x} + \rho v \frac{\partial v}{\partial y} + \rho w \frac{\partial v}{\partial z} = -\frac{\partial p}{\partial y} + \frac{\partial}{\partial x}(\mu \frac{\partial v}{\partial x}) + \frac{\partial}{\partial y}(\mu \frac{\partial v}{\partial y}) + \frac{\partial}{\partial z}(\mu \frac{\partial v}{\partial z}) + S_y \tag{3.11}$$

$$\rho \frac{\partial w}{\partial t} + \rho u \frac{\partial w}{\partial x} + \rho v \frac{\partial w}{\partial y} + \rho w \frac{\partial w}{\partial z} = -\frac{\partial p}{\partial z} + \frac{\partial}{\partial x}(\mu \frac{\partial w}{\partial x}) + \frac{\partial}{\partial y}(\mu \frac{\partial w}{\partial y}) + \frac{\partial}{\partial z}(\mu \frac{\partial w}{\partial z}) + S_z \tag{3.12}$$

The equations of momentum are coupled by the velocity components, which makes the solution of these to be dependant on each other. With reference to the general transport equation, the momentum equation can be obtained if the general variable is assigned as $\phi = \mathbf{u}$, the diffusive coefficient is assigned as $\Gamma = \mu$, and the source S_ϕ contains the forces in the momentum sources $\mathbf{S_M}$ (compounded by the secondary viscous stress contributions of μ and the gravitational force $\mathbf{f}$) and the pressure gradient $-\nabla p$.

3.1.3 Energy equation

The energy PDE describes that the rate of increase of energy is equal to the net rate of added heat plus the rate of work done on the fluid particle (Thermodynamics' first law). The added heat is defined by $\nabla \cdot \mathbf{q}$, while the work rate is defined by the forces in the momentum equation multiplied by the velocity $\mathbf{u}$.

$$\frac{\partial(\rho E)}{\partial t} + \nabla \cdot (\rho \mathbf{u} E) = \nabla \cdot \mathbf{q} - \nabla \cdot (p\mathbf{u}) + \nabla \cdot (\boldsymbol{\tau} \cdot \mathbf{u}) + \mathbf{u} \cdot \mathbf{f} \tag{3.13}$$

Energy E and pressure p can be expressed as the enthalpy H in a system. The enthalpy is compunded by the static enthalpy H_{static} and the kinetic energy $\frac{|\mathbf{u}|^2}{2}$. For ideal gases, the static enthalpy is the product between the specific heat c_p and the temperature T.

$$\rho E + p = \rho H = \rho \left(H_{\text{static}} + \frac{|\mathbf{u}|^2}{2} \right) = \rho \left(c_p T + \frac{|\mathbf{u}|^2}{2} \right) \tag{3.14}$$

In the case of solid bodies, there is no mass or momentum transfer ($\mathbf{v} = 0$), and therefore the energy is represented by the enthalpy and the rate of increase of energy is equal to the added heat.

$$\frac{\partial(\rho c_p T)}{\partial t} = \nabla \cdot \mathbf{q} \tag{3.15}$$

The heat flux vector $\mathbf{q}$ comprises both the conductive and the convective heat transfer which are modeled with Fourier's and Newton's laws respectively.

$$\mathbf{q} = -k\nabla T + h(T - T_\infty) \tag{3.16}$$

Where k is the material thermal conductivity, h is the local heat transfer coefficient and T_∞ is the characteristic temperature of the surrounding.

Depending on the driving force that causes the fluid motion, the convection can be natural or forced.

- Natural convection: it takes place when the motion is originated by the variation of density in the fluid caused by temperature. Warm fluid decreases density and moves upwards, whiles it is substituted by cold fluid.
- Forced convection: it takes place when the fluid is forced to move, for instance by external mechanical energy (e.g. supplied by a fan), transferring velocity to the fluid and increasing heat transfer.

The convection heat transfer coefficient h determines whether natural or forced convection is dominant. This coefficient is a function of non-dimensional parameters (see section 3.3.4).

3.2 RANS turbulence model

Turbulence can be defined as the chaotic change in flow properties generated by shear stress. To account for turbulence, it is necessary to decompose the instantaneous fields into mean and fluctuating components. By averaging the implementation of the fluctuating and mean components for properties in the instantaneous governing equations, Reynolds Averaged Navier-Stokes (RANS) equations are expressed in terms of the mean properties of the flow and the Reynolds stresses, which account for the turbulence fluctuations.

$$\tau_{xx} = \overline{u'^2}\,;\ \tau_{yy} = \overline{v'^2}\,;\ \tau_{zz} = \overline{w'^2}\,;\ \tau_{xy} = \tau_{yx} = \overline{u'v'}\,;\ \tau_{xz} = \tau_{zx} = \overline{u'w'}\,;\ \tau_{yz} = \tau_{zy} = \overline{v'w'} \tag{3.17}$$

In the Reynolds Averaged Navier-Stokes (RANS) equations, eddy viscosity models are used, in which the effect of Reynolds stresses are governed by the same physics as the viscous stresses, which are given by the Newton's Law in incompressible flow with constant viscosity. The main assumption made in RANS models is the Boussinesq hypothesis, in which the unknown Reynolds stresses are proportional to the mean rates of deformation [15].

$$\tau_{ij} = -\rho u_i' u_j' = \mu_t \left(\frac{\partial U_i}{\partial x_j} + \frac{\partial U_j}{\partial x_i} \right) - \frac{2}{3}\rho k \delta_{ij} \tag{3.18}$$

To determine the unknown Reynolds stresses, closure is provided by functions that contain empirical constants relating the turbulence to the mean flow. The turbulent viscosity μ_t in the Boussinesq hypothesis, which determines the effect of turbulence on the mean properties of the flow, can be obtained through the kinetic energy k and the dissipation rate of kinetic energy ϵ to thermal energy. A popular model to solve for the kinetic energy and its dissipation rate are the k-ϵ equations. The realizable k-ϵ model is used in the present research, which provides accuracy for complex flows, such as swirling and separating flows, ensuring that the turbulence kinetic energy is always positive and physically realizable. These equations are shown below [19].

Turbulent Kinetic Energy (k) equation:

$$\frac{\partial(\rho k)}{\partial t} + \frac{\partial(\rho k u_i)}{\partial x_i} = \frac{\partial}{\partial x_j}\left[\left(\mu + \frac{\mu_t}{\sigma_k} \right) \frac{\partial k}{\partial x_j} \right] + P_k - \rho\varepsilon \tag{3.19}$$

Turbulent Dissipation Rate (ϵ) equation:

$$\frac{\partial(\rho \varepsilon)}{\partial t} + \frac{\partial(\rho \varepsilon u_i)}{\partial x_i} = \frac{\partial}{\partial x_j}\left[\left(\mu + \frac{\mu_t}{\sigma_\varepsilon} \right) \frac{\partial \varepsilon}{\partial x_j} \right] + C_{\varepsilon_1}\frac{P_k}{k}\varepsilon - C_{\varepsilon_2}\frac{\rho\varepsilon^2}{k} \tag{3.20}$$

Where P_k:

$$P_k = \rho \left(-\varepsilon + \frac{\partial}{\partial x_j}\left[\left(\mu + \frac{\mu_t}{\sigma_k} \right) \frac{\partial k}{\partial x_j} \right] + 2\mu_t S_{ij} S_{ij} \right) \tag{3.21}$$

3.2.1 Turbulence wall treatment

In the k-ϵ models, it exists a limitation to properly capture the turbulence near the fluid domain boundary walls, where k and ϵ are approximately zero. Therefore a two-layer model is applied, in order to set two regions of turbulence study. The outer region, which can be called bulk region, belongs to the inner volume away from the boundary walls. In the near wall region, which contains the viscous sublayer and buffer layer, turbulence is affected by the viscous effects.

For the turbulent viscosity to account for the proximity to the wall, a proximity factor is defined as f_λ. The turbulent viscosity near the wall is modeled with an expression dependent in the Reynolds wall distance. Away from the wall, the turbulent viscosity is modeled with the k-ϵ original equations. In the regions close to the boundary walls, the proximity factor sets the proportion of bulk and near-wall turbulent viscosities to calculate an appropriate value [25,26].

$$\mu_t = f_\lambda \mu_t^{bulk} + (1 - f\lambda)\mu_t^{near-wall} \tag{3.22}$$

$$\mu_t^{near-wall} = 0.42\mu Re_d C_\mu^{1/4}\left[1 - \exp\left(-\frac{Re_d}{70}\right)\right] \tag{3.23}$$

$$\mathrm{Re}_d = \frac{\rho\sqrt{k}y}{\mu} \tag{3.24}$$

The dissipation rate near the wall is calculated as an expression function of k and length scale l_ϵ.

$$\epsilon_{\text{near-wall}} = \frac{k^{3/2}}{l_\epsilon} \tag{3.25}$$

$$\epsilon = C_l y\left[1 - \exp\left(-\frac{\mathrm{Re}_d}{2C_l}\right)\right] \tag{3.26}$$

In the present research, the meshing of the domain of study is aimed to be fine enough in the viscous sublayer to capture the turbulence effects by adapting the turbulent viscosity in the k-ϵ model as indicated above. Therefore, no additional wall treatment would be necessary to properly capture the behaviour of the flow.

An all y+ approach is used in the CFD software, in which the modelling of turbulence is selected automatically depending on the refinement of the mesh near the wall and the corresponding y+.

3.2.2 Hidraulic boundary layer

The particles of fluid that are in contact with a boundary wall acquire zero velocity while the adjacent layers of particles which are located above the surface increase their velocity progressively caused by the shear stress in the direction of the fluid flow. This is defined as the viscous sublayer, where the flow is mainly affected by molecular viscosity. Further from the wall, out of the viscous sublayer, the velocity of the particles increases until the speed distribution becomes constant at the free stream velocity. This part of the boundary layer is turbulent and the velocity profile follows a logarithmic behaviour.
In order to capture the mentioned effects, different formulation is used depending on the first mesh cell height on the wall. The cell height is related to the dimensionless distance y+ from the cell centroid to the wall [18].

$$y^{+} = \frac{u_{\tau} y}{\nu} \; ; \; u_{\tau} = \sqrt{\frac{\tau_w}{\rho}} \tag{3.27}$$

3.2.3 Thermal boundary layer

There is a thermal boundary layer if the temperature of the free fluid flow and the temperature of the surface in question are different. The particles which are in contact with the surface get into thermal equilibrium with it. The particles which are in adjacent layers have an energy exchange, generating temperature gradients. The region of fluid where these temperature gradients exist, and therefore heat exchange by convection, is known as the thermal boundary layer. In order to capture the mentioned effects, different formulation is used depending on the first mesh cell height on the wall. The cell height is related to the dimensionless distance y* from the cell centroid to the wall.

$$y^{*} = \frac{u_{\tau} y}{\nu} \; ; \; T^{*} = \frac{T_{\infty} - T_w}{T - T_w} = \frac{\rho C_p (T_{\infty} - T_w)}{q_w} \tag{3.28}$$

3.3 Air physics function of temperature

3.3.1 Boussinesq model

The Boussinesq approximation is used to model the behavior of fluids with density variations, such as in the case of natural convection. The assumption is that the density variations in the fluid are small and thus can be approximated by a linear approximation in the Navier-Stokes equations. To do so, the density is expressed as the sum of a reference value ρ_0 and a small variation $\Delta\rho$.

$$\rho = \rho_0 + \Delta\rho \tag{3.29}$$

Introducing this new expression for the Navier-Stokes equations, the density can be assumed constant to the reference value ρ_0 in the temporal and convective terms and expressed in terms of the Buoyancy force $\rho g/\rho_0$.

Conservation of mass:

$$\nabla \cdot \mathbf{u} = 0 \tag{3.30}$$

Conservation of momentum:

$$\frac{\partial \mathbf{u}}{\partial t} + \mathbf{u} \cdot \nabla \mathbf{u} = -\frac{1}{\rho_0}\nabla p + \nu \nabla^2 \mathbf{u} + \frac{\rho g}{\rho_0} \tag{3.31}$$

The movement of the fluid caused by temperature difference can be modeled in the gravitational Buoyancy force term. To do so, the thermal expansion coefficient is included as a linear approximation.

$$\beta = -\frac{1}{\rho_0}(\frac{\partial \rho}{\partial T}) \approx -\frac{1}{\rho_0}\frac{\rho - \rho_0}{T - T_0} \tag{3.32}$$

$$\rho \approx \rho_0[1 - \beta(T - T_0)]g \tag{3.33}$$

Which can be included in the Buoyancy force term accounting for the variation of the density. The momentum equation finally takes the form shown below [22].

$$\frac{\partial \mathbf{u}}{\partial t} + \mathbf{u} \cdot \nabla \mathbf{u} = -\frac{1}{\rho_0}\nabla p + \nu \nabla^2 \mathbf{u} + [1 - \beta(T - T_0)]g \tag{3.34}$$

This results in a model which accounts for the movement of warm air upwards and cold air downwards by deleting the instability of the non-linear original Navier-Stokes equations.

3.3.2 Sutherland's Law

Sutherland's Law is commonly used to describe the variation of viscosity with temperature for gases at low to moderate pressures, and is based on the assumption that gas molecules behave as rigid spheres with attractive forces between them [27].

$$\mu(T) = \frac{C_1 T^{\frac{3}{2}}}{T + C_2}, \tag{3.35}$$

where μ is the dynamic viscosity, T is the absolute temperature in Kelvin, and C_1 and C_2 are constants that depend on the particular gas being considered.
Sutherland's Law for thermal conductivity is also based on the assumption that gas molecules behave as rigid spheres with attractive forces between them. It is commonly used to describe the variation of thermal conductivity with temperature for gases at low to moderate pressures:

$$k(T) = \frac{C_3 T^{\frac{3}{2}}}{T + C_4}, \tag{3.36}$$

where k is the thermal conductivity, T is the absolute temperature in Kelvin, and C_3 and C_4 are constants that depend on the particular gas being considered.

3.3.3 Specific heat capacity polynomial

Specific heat capacity is the amount of heat energy required to raise the temperature of a unit mass of a substance by one degree Celsius (or Kelvin) without a phase change occurring. It is denoted by the symbol c_p and has units of J/(kg · K) or J/(kg · °C).

The specific heat capacity for the air varies with temperature [28]. This behavior can be defined by a polynomial function of temperature.

$$\mathbf{a} = [a_5, a_4, a_3, a_2, a_1, a_0] \tag{3.37}$$

$$\mathbf{a} = [-1.6719E - 10, 2.41419E - 7, -1.37005E - 4, 3.858132E - 2, 5.429752, 1312.898067] \tag{3.38}$$

$$c_p(T) = a_5 \cdot T^5 + a_4 \cdot T^4 - a_3 \cdot T^3 + a_2 \cdot T^2 - a_1 \cdot T + a_0 \; [J/(kg \cdot K)] \tag{3.39}$$

The polynomial coefficients have been obtained by polynomial regression of literature data.

3.3.4 Convection coefficient for heat transfer

The Prandtl number is a dimensionless parameter that relates the momentum diffusivity to the thermal diffusivity of a fluid. It is often used in the context of convective heat transfer.

$$Pr = \frac{\text{Thermal diffusivity}}{\text{Momentum diffusivity}} = \frac{\alpha}{\nu} = \frac{\mu c_p}{k} \tag{3.40}$$

The Reynolds number is a dimensionless quantity that characterizes the flow regime of a fluid. It is defined as the ratio of inertial forces to viscous force. In words, the Reynolds number is a measure of how turbulent or laminar a fluid flow is. A higher Reynolds number indicates a more turbulent flow, while a lower Reynolds number indicates a more laminar flow.

$$\mathrm{Re} = \frac{\text{Inertial forces}}{\text{Viscous forces}} = \frac{\rho L}{\nu} = \frac{\rho u L}{\mu} \tag{3.41}$$

The Grashof number represents the ratio between the buoyancy force due to spatial variation in fluid density (caused by temperature differences) to the restraining force due to the viscosity of the fluid.

$$\mathrm{Gr} = \frac{\text{Buoyancy forces}}{\text{Viscous forces}} = \frac{gL^3\beta\Delta T}{\nu^2} \tag{3.42}$$

The Nusselt number is the ratio of convective to conductive heat transfer across a boundary. The convection and conduction heat flows are parallel to each other and to the surface normal of the boundary surface and are all perpendicular to the mean fluid flow in the simple case.

$$Nu = \frac{\text{Convective heat transfer}}{\text{Conductive heat transfer}} = \frac{hL}{k} \tag{3.43}$$

Therefore the convection coefficient h can be approximated by $Nu(Re, Pr, Gr) \cdot k/L$ [20].

3.4 Radiation

Radiation is the heat transfer by electromagnetic exchange between bodies at different temperatures. The energy does not need a physical continuum to be transmitted by radiation.

3.4.1 Surface to surface model

Up until now, the behavior of conduction and convection of properties within the fluid have been modelled through transport governing equations. Radiation is a phenomena related with the geometry of the boundary surfaces of the domain. For a black body, considered a perfect radiation emitter, the emitted radiation heat flux is expressed as follows.

$$Q_{rad} = \sigma T^4 \ ; \ q_{rad} = \sigma A T^4 \tag{3.44}$$

In CFD the heat flux across the boundaries of the fluid domain requires of a separate model. The grey thermal radiation model is applied. In such a model, the heat flux emitted by a black body is multiplied by ϵ, which is assumed to be independent of the radiation's wavelength. This accounts for the behaviour of different materials towards radiation, by specifying an imperfect emission ϵ of radiation [21].

$$q_{rad} = \epsilon \sigma A T^4 \ ; \ 0 < \epsilon < 1 \tag{3.45}$$

The radiation fractions can be defined as follows.

1. Absortivity α: it is the absorbed fraction of all the incident radiant power.
2. Transmitivity τ: it is the transmitted fraction of all the incident radiant power through the solid.
3. Reflectivity ρ: it is the reflected fraction of all the incident radiant power.

$$\alpha + \tau + \rho = 1 \tag{3.46}$$

And by Kirchoff's law, $\alpha = \epsilon$.

$$\epsilon + \tau + \rho = 1 \tag{3.47}$$

For incident radiation on a surface k, the heat flux balance can be written as follows.

$$q_{k,out} = q_{k,in} \cdot \rho + q_{k,in} \cdot \tau + \epsilon_k \sigma T^4 \tag{3.48}$$

After incidence with a surface, the outing radiant flux can be received by all the other surfaces in the fluid domain. To account for this, the view factors are computed in accordance to the geometry of the surrounding surfaces. The view factors can be defined as the fraction of radiant flux that leaves surface j which is received by surface k. The total sum of factor views leaving a surface must be 1 by energy conservation.

$$\sum_{k=1}^{n} F_{jk} = 1 \tag{3.49}$$

$$F_{j1} + F_{j2} + F_{j3} + \ldots + F_{jn} = 1 \tag{3.50}$$

The integral to obtain the view factors accounting for the geometry of the surrounding surfaces is expressed as follows.

$$F_{jk} = \iint_A \frac{\cos(\theta_j)\cos(\theta_k)}{r^2} dA \tag{3.51}$$

The radiant flux received by surface k, can be expressed in terms of the factor views as shown below.

$$q_{k,in} = \sum_{j=1}^{n} F_{jk} \cdot q_{j,out} \tag{3.52}$$

Finally, the outing radiant heat flux on a surface k can be expressed in terms of the radiation received by surrounding surfaces by means of the view factors.

$$q_{k,out} - [\sum_{j=1}^{n} F_{jk} \cdot q_{j,out}] \cdot (\rho + \tau) = \epsilon_k \sigma T^4 \tag{3.53}$$

Following this relationship, the CFD software obtains a radiosity vector, containing all the radiant heat fluxes outing the cells at the fluid boundary walls. These radiant heat fluxes are added to the governing equations of transport within the fluid.

3.4.2 Solar loads

In the current simulation, the main source of radiation is the solar load. The radiant energy of the sun can cause the surfaces of a car cabin to increase above the ambient temperature. Therefore, its modeling is of significant importance.

The solar load modeling can be divided by a direct radiant flux and a diffuse radiant flux, measured in W/m^2. The direct radiant flux is originated directly by the incident rays of the sun, while the diffuse radiant flux is originated by the reflected sun rays by obstacles such as clouds.

In order to account for the orientation of the solar load, azimuth θ and altitude α angles are specified with regards to the target object. The azimuth angle is the one located at the horizontal plane, while the azimuth is the one located at the vertical plane. In this way, the direction of the direct sunlight with regards to the target object is specified.

3.5 Transport of CO_2 in the air

An interesting part of the present research is the study of the propagation of carbon dioxide inside the air domain.

The concentration of carbon dioxide as a gas within the air can be treated as a passive scalar in the CFD software, which means that the gas will be transported as a property of the fluid by effects of convection and conduction without making an effect on its motion.

An additional transport equation for the passive scalar is therefore required. The degree of mixing with the surrounding air depends on the Schmidt number, which is defined by the relation between the viscosity and the molecular diffusivity of the passive scalar with the surrounding air.

$$Sc = \frac{\text{Momentum diffusivity}}{\text{Passive scalar mass diffusivity}} = \frac{\nu}{D} \tag{3.54}$$

The assigned Schmidt number for the carbon dioxide within the surrounding air can be considered 1 according to the literature [23].

4

Methods

4.1 Case study summary

The present research aimed to simulate, using Star CCM+ as CFD software, a series of heat transfer mechanisms that could take place in a car cabin. Such mechanisms were evaluated by introducing them sequentially until a complete global scenario was achieved. The global scenario contemplated the heat transfer effects of exterior and interior air temperature by convection effects, heat conduction across the cabin boundaries, solar load radiation from the sun, and the metabolic heat and CO_2 load of passengers inside the cabin. A representative scene of the final global scenario is shown below in Figure 4.1.

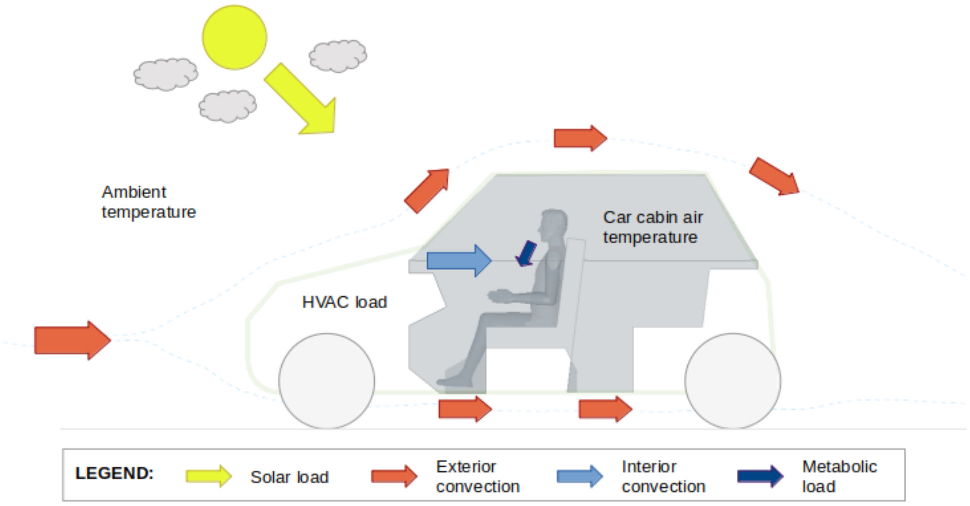

Figure 4.1: Schematic representation for the global scenario object of study

A summary of all the studied cases is presented in Table 4.1 at the beginning of this chapter in order to prepare the reader for a better understanding of the structure of the present analysis.

Table 4.1: Summary table for all the study cases in the present research.

	Title	Purpose	Characteristic boundary conditions
Case 1	Airflow simulation without heat transfer.	Resolve the inner airflow patterns inside the car cabin, produced by the air jets from the HVAC. Find the proper parameters for the car cabin mesh using this scenario as the reference.	Total air mass flow = 68.5 g/s. Proportion of 0.8 to the top inlets and 0.2 to the bottom inlets.
Case 2	Effect of thermal resistance at boundaries.	Consider that the car is moving at 32 km/h at ambient temperature of 43ºC, air inlet temperature from the HVAC at 7ºC, and no solar load. The insulation is considered adiabatic.	Thermal resistance is considered infinite at all boundaries but the windshield and windows.
Case 3	Effect of thermal resistance at boundaries.	Consider that the car is moving at 32 km/h at ambient temperature of 43ºC, air inlet temperature from the HVAC at 7ºC, and no solar load. The insulation is not adiabatic.	Thermal resistance is considered 0.46 $m^2 \cdot$ K/W at most boundaries but the windshield and windows.
Case 4	Effect of thermal resistance at boundaries.	Consider that the car is moving at 32 km/h at ambient temperature of 43ºC, air inlet temperature from the HVAC at 7ºC, and no solar load. There is no insulation.	Thermal resistance is considered 0.06 $m^2 \cdot$ K/W at most boundaries but the windshield and windows.
Case 5	Effect of solar load.	A moderate solar load is added at 180º azimuth angle and at 45º altitude angle.	Direct solar flux of 500 W/m^2 and diffuse solar flux of 250 W/m^2.
Case 6	Effect of solar load.	An intense solar load is added at 180º azimuth angle and at 45º altitude angle.	Direct solar flux of 1000 W/m^2 and diffuse solar flux of 500 W/m^2.
Case 7	Effect of air inlet distribution.	The total air mass flow is now applied at the top inlets to improve the cooling distribution, with an intense solar load at 180º azimuth angle and at 45º altitude angle.	Direct solar flux of 1000 W/m^2 and diffuse solar flux of 500 W/m^2. Total air mass flow = 68.5 g/s at top inlets.
Case 8	Time-step sensitivity analysis.	Understand the temporal evolution of temperature at probe points of interest. A transient time-step study applied using the conditions in Case 7.	Unsteady simulation for case 7.
Case 9	Effect of total air mass flow rate including the driver.	Understand the stationary levels of temperature and CO_2 concentration at different air mass flow rates and with the presence of a driver. The two levels of solar loads are simulated.	Addition of a driver with skin temperature of 34ºC and exhaled air at 37ºC and 40000 ppm of CO_2. Addition of 430 ppm CO_2 at the air inlets. Variation of total air mass flow rate.
Case 10	Transient analysis on air temperature and quality.	Understand the transient levels of temperature and CO_2 concentration at different air mass flow rates of interest with the presence of a driver. The two levels of solar loads are simulated.	Unsteady simulation for case 9 at air mass flow rates of interest.

4.2 Geometry

The geometry of study in Figure 4.2 represented a generic interior of a car cabin. The geometry can be understood as a volume enclosed by surface boundaries. The volume is related to the air volume inside the cabin, in which the fluid will transport its properties by mechanisms of conduction and convection. The surface boundaries are related to the inner surfaces of the car cabin, which belong to parts such as the roof, windows, doors, floor, and interior elements. Surface boundaries will exchange heat by radiation in the case of existing solar load.

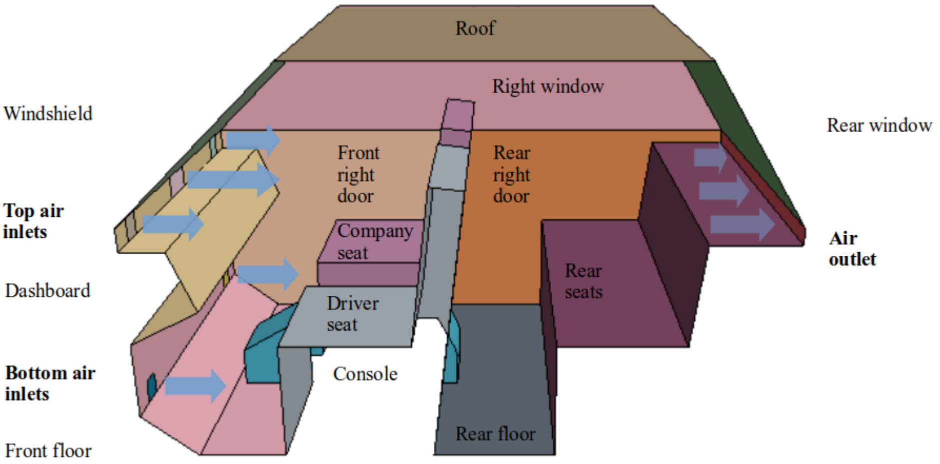

Figure 4.2: Generic geometry of the car cabin and its boundary names

The dimensions of the cabin were 2.41 m of length, 1.44 m of width and 1.5 m of height. The elements inside the cabin were simplified with the aim to conduct a generalized study which could be linked to different car models.

The surface boundaries were organized in groups depending on the nature of their properties:

- Low thermal resistance walls: it groups the boundaries which represent the windows, which are modeled by low thermal resistance offered by the glass. Therefore, this group enables the highest heat exchange within the cabin. The windshield, right window, left window and rear window belong to this group.
- Standard thermal resistance walls: it groups the boundaries which represent walls with a finite thickness which are made by a combination of layers of materials such as metals, plastics and air gaps. These walls offer certain thermal resistance and insulate the car cabin from the outer conditions. The roof, doors, rear floor and console are included in this group.
- High thermal resistance walls: it groups the boundaries in the front of the cabin under the windshield. These boundaries are separated from the outer conditions by the frontal of the car, including all the elements under the bonnet. This setting justifies a high thermal resistance associated with these boundaries. The front wall, compounded by the dashboard and the front front floor, belongs to this group.

- Seats: front and rear seats are related to this group. These boundaries are treated as adiabatic walls as they are not facing the outer conditions and in steady state there would not be heat exchange with the interior air.

- Inlets: it is conformed by the air inlets at the front of the cabin. There are three air inlets at the top at the dashboard, and two at the bottom at the front wall. The area of a single air inlet is 77.45 cm^2, and these are located to the top and bottom laterals. There is a central top air inlet, which has double the area, i.e. 154.85 cm^2.

- Outlet: there is a single outlet above the rear seats with an area of 890 cm^2.

A representation of the surface groups is offered below in Figure 4.3.

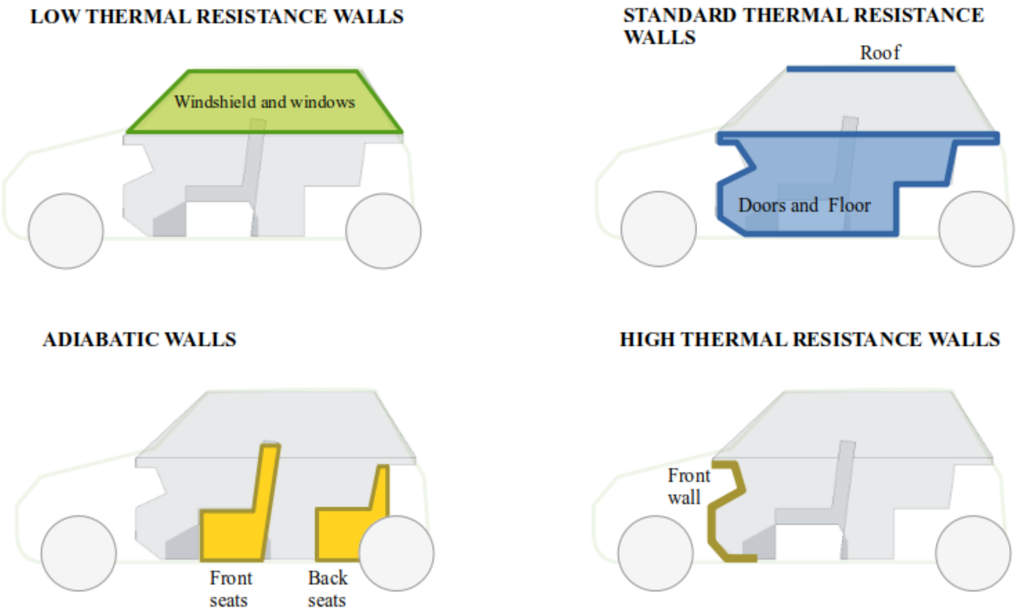

Figure 4.3: Visual identification for the groups of boundary walls

The dimensions of the elements within the cabin, as well as the area of air inlets, were generalized and were representative of a standard car. Further discussion on how the air inlets relate to a real scenario can be found in the following subsection 4.3.

4.3 Physics continua and boundary conditions

The physics continua models and the boundary conditions applied to the volume boundary surfaces depend on the case of study. In this subsection, all the case of study along with the used physics models and boundary conditions are introduced. The boundary conditions are applied differently to each group of surface boundaries described in the previous subsection.

4.3.1 Case 1: Airflow simulation without heat transfer

4.3.1.1 Mesh setting

In order to solve for the fluid properties of interest, a discretization of the air domain is necessary.

The density of cells in different regions of the air domain can have an influence on the solution of the properties of interest. This phenomenon can be produced if the fluid property gradients (i.e. change of value in space) are too high to be captured by a certain density of cells. Therefore, a mesh sensitivity analysis is required in order to validate that the obtained solutions are mesh independent.

This initial meshing stage was particularly important in the present research. No experimental data for a specific case was available. Therefore, a comprehensive mesh study was considered valuable in order to make sure that the results were valid and mesh-independent.

A good way to approach the mesh sensitivity analysis is to first understand the different type of mesh geometries used in the discretization.

- Inner volume mesh: the volume within the surface boundaries of the car cabin is discretized using polyhedral cells. These type of cell, if compared to others such as tetrahedrons, have the advantage that adapt better to complex geometries by achieving better cell quality and they also provide a lower cell count, reducing thus the computational cost of the calculations.

- Near wall volume mesh: the volume nearby the surface boundaries of the car cabin is usually meshed using prism layer cells. The purpose of these prism layers is to capture the gradients within the boundary layers on the walls for properties such as velocity and temperature. The prism layers grow gradually in size in a normal direction to the boundaries. The total thickness of the prism layers must be sufficient to capture the gradient produced on the walls. The height of the first cell to the wall determines the value of y+, leading to different boundary layer computations depending on its value [18].

- Surface mesh at the wall: the mesh at the wall is compounded by the prism layers' base cells, except at the inlets and outlet. It is important to note that the size of the surface mesh has a direct effect on the size of the prism layers and the volume mesh. The ideal scenario in meshing is a smooth transition in cell size between meshes.

The approach followed by the present research was to consider a refined mesh to achieve a y+<1 at all the walls, assuming a fine mesh at the boundaries to account for the high velocity and temperature gradients at the boundaries. A mesh sensitivity study was carried out by varying the refinement levels at the prism layers and volume mesh. The velocity values were monitored using line probes, which enable the plot of velocity profiles for comparison between meshes. Figure 4.4 contains the main concepts described in this subsection.

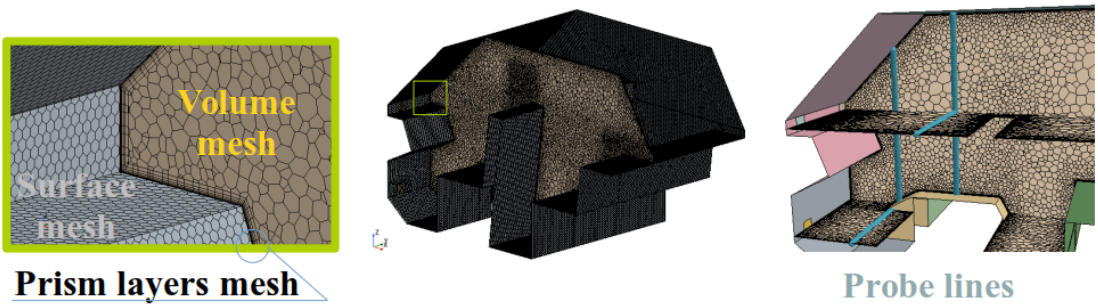

Figure 4.4: Types of meshes used within the car cabin and line probes used in the sensitivity analysis

4.3.1.2 Simulation setting

Since no heat transfer is studied in the present case, only the equations of continuity, momentum, and turbulence are solved. Therefore, the air properties do not depend on the temperature.

To model the physics of the air, a constant density was set to 1.184 $\mathrm{kg/m^3}$ and the dynamic viscosity was set to $1.855 \cdot 10^{-5}$ Pa · s. This was a steady-state case that uses the Reynolds Averaged Navier-Stokes equations for continuity and momentum, the Realizable k-epsilon for turbulence, and the Segregated flow approach for the solution of the equations [15]. The all-y+ wall treatment was used to account for the generation of hydraulic boundary layers nearby the wall boundaries.

A pressure reference of 101325 Pa was used to account for atmospheric conditions.

With respect to the boundary conditions applied to the surface boundary groups, they were divided into the following ones:

- Inlets: an air mass flow rate is specified for each inlet. The velocity of the air at the inlets is defined by the air mass flow rate and the inlet area.
- Outlet: the air which is introduced inside the domain through the inlets will finally exit the car cabin by the specified outlet.
- Walls: a non slip condition is applied to all the boundary surfaces of the car cabin, with exception of the inlet and outlet boundaries. This allows to account for the gradient of velocities generated at the boundary layers nearby the walls by shear stresses.

The value of air mass flow rate was set taking into account the existing literature as a reference.

In the literature [12], the air mass flow rate measurement at air vents within a real car cabin was carried out. The measurements were conducted at different external temperatures and HVAC programs. The total air mass flow for the summer case in the literature was taken as a reference in the present research, in which the outer temperature was 30°C with a solar load of 800 W/m^2, and the HVAC program was set to AUTO to reach a cabin temperature of 23°C. In this case, the total air mass flow was measured to be approximately 68.5 g/s, but the temperature at the air inlets was unknown.

Comparing the air mass flow rate distributions in the literature of reference and in the present research:

- The proportion of total air mass flow rate in the literature (68.5 g/s) is 0.6 to the dashboard vents, 0.2 to the windshield defroster vents, 0.15 to the rear seats and 0.05 to the feet vents. This can be summarized as a proportion of 0.8 to the top front vents with a total inlet area of 318.5 cm^2, 0.15 to the rear vents with a total inlet area of 54 cm^2 and a 0.05 to the feet vents with a total inlet area of 136.5 cm^2.

- The total air mass flow rate in the present research was also set to 68.5 g/s, applying a proportion of 0.8 to the top inlets with a total inlet area of 309.8 cm^2, and a proportion of 0.2 to the bottom inlets with a total inlet area of 154.9 cm^2.

- There was a reasonable agreement between total air mass flow distribution and inlet area to consider the present research representative of a real scenario.

An airflow simulation without heat transfer was useful to perform a mesh sensitivity analysis as well as to study the airflow general patterns that take place inside the cabin. The discretization of the volume of air domain can have an effect on the velocity magnitude of the airflow, which can later have an effect on the transport of temperature by convection within the cabin. The mesh that was deemed suitable at the end of the mesh study was used for all subsequent analyses.

4.3.2 Case 2 to 4: Effect of thermal resistance at boundaries

Conduction and convection heat transfer effects were taken into account for the first time in the present case. Therefore, the equation of energy was also considered in addition to the continuity, momentum, and turbulence equations. A segregated fluid temperature approach is used to solve the energy equation.

The air was also considered to have constant density. The movement of hot air upwards and cold air downwards due to temperature changes was simulated through the Boussinesq model [22], which takes the effect of gravity into account. The properties of the air function of its temperature were considered using Sutherland's law for the dynamic viscosity and the thermal conductivity, and a polynomial in temperature for the specific heat.

An initial pressure condition was imposed by considering the hydrostatic pressure accounting for the gravity effect. The value is the density times gravity and cells' centroid height.

With respect to the boundary conditions applied to the surface boundary groups, they can be divided in the following ones:

- Inlets: in addition to the last case, the air inlet temperature was specified.
- Outlet: the air which was introduced inside the domain through the inlets will finally exit the car cabin by the specified outlet.
- Walls: in addition to the no-slip condition, several thermal specifications are defined at the boundaries. If the wall is considered adiabatic, no heat flux is crossing the boundary. If the wall is considered a convective wall then the exterior temperature to the boundaries (ambient), the outer heat transfer coefficient, and the thermal resistance of the boundary must be specified.

In the present research, further references are taken from literature in order to set a realistic heat transfer scenario.

In literature, a summer case scenario was simulated by means of CFD. Among the studied cases, the temperature conditions of a steady-state simulation are taken as a reference for this research. The solar load was 1000 W/m^2, the outer ambient temperature was 43°C, the air inlet temperature was 7°C, and the vehicle speed was 32 km/h [13,14].

For the current research case, only the temperatures were used as a reference. In this way, a first realistic summer car cabin cool-down scenario was simulated. The solar load effect was studied later in the coming research cases. For the total air mass flow rate, the previous 68.5 g/s with the same inlet distribution was considered.

The fact that the car is moving at 32 km/h, implies that there is an effect of forced convection from the external air to the walls of the cabin. Therefore, a convection coefficient accounting for the vehicle speed must be specified in order to simulate the heat transfer between the external air and the cabin walls. For the walls which are in contact with the external air, the approximated heat transfer coefficient is 46.26 W/(K $\cdot$ m^2) calculated using the equation given by literature [13,14].

$$h = 1.163 \cdot (4 + 12 \cdot \sqrt{\mathbf{v}}) \tag{4.1}$$

Where $\mathbf{v}$ is the velocity of the car.

Not only the external convection coefficient must be specified, but also the thermal resistance of the boundaries exposed to external forced convection. The thermal resistance of the boundaries is defined by the different types of material layers. The thermal resistance of a boundary is therefore a function of the thickness of the layers and the thermal conductivity of the materials.

The total resistance of a multilayered wall can be calculated as the sum of the thermal resistance for each layer. The thermal resistance per area unit in each layer is the result of dividing the layer thickness by its thermal conductivity.

A representation of the different thermal resistance walls (Figure 4.3) is shown below together with a table (Table 4.2) containing approximate thickness and thermal conductivity values depending on the materials in accordance with [16]. Table 4.3 sums up the resulting thermal resistances at each boundary group for each of the three analyzed cases.

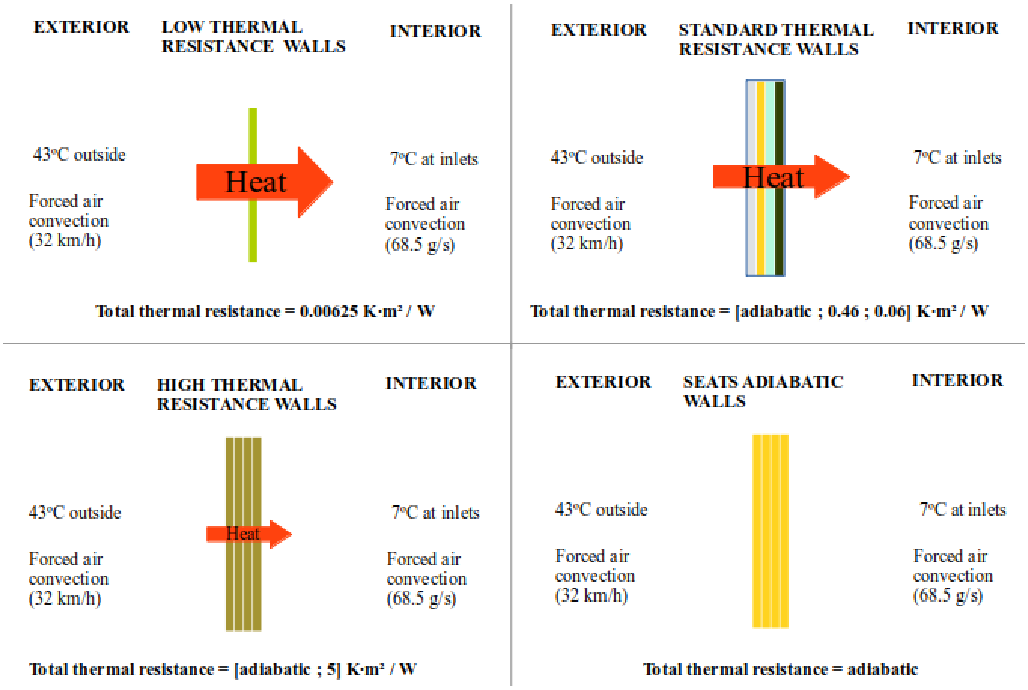

Figure 4.5: Thermal properties for the wall boundary conditions based on literature [14,15]

Table 4.2: Thickness, conductivity and thermal resistance associated to layer materials in accordance to literature [17,18]

Windows	Glass	Roof, doors, and floor	Steel	Inner panel	Insulation	Plastic cover
Thickness [m]	5e-3	Thickness [m]	7.5e-4	2e-3	20e-3	2e-3
Conductivity [W/(K · m)]	0.8	Conductivity [W/(K · m)]	64	0.04	0.05	0.13
Resistance [K · m^2/W]	6.25e-3	Resistance [K · m^2/W]	1.17e-5	5e-2	4e-1	1.5e-2

Table 4.3: Cases set to study the effect of the thermal insulation in standard thermal resistance walls

Thermal resistance [K · m² / W]	**Low thermal resistance walls**	**Standard thermal resistance walls**	**High thermal resistance walls**	**Seats**
Case 2	0.00625	Adiabatic	Adiabatic	Adiabatic
Case 3	0.00625	0.06	5	Adiabatic
Case 4	0.00625	0.46	5	Adiabatic

In the present case of study, the influence of thermal resistance in the standard thermal resistance boundary group is studied. Three different cases are analyzed.

- Case 2: all the boundaries are considered adiabatic with exception of the low thermal resistance walls. This group is compounded by boundaries made of glass. These are the windshield, left window, right window and rear window.
- Case 3: only the seats are considered adiabatic this time. The standard thermal resistance walls are compounded by steel, inner plate and plastic layers without any insulation. This group is compounded by the roof, doors and floor of the car cabin.
- Case 4: only the seats are considered adiabatic this time. The standard thermal resistance walls include a layer of insulation.

4.3.3 Case 5 and 6: Effect of solar load.

Solar radiation was taken into account for first time in combination with conduction and convection in Case 5 and 6. The radiation model included gray thermal radiation, solar loads and surface to surface. The air properties changed in function of the temperature using the models specified in the previous case of study.

The only additional condition to this new case is the presence of solar loads of different intensity. The amount of insulation considered at the standard thermal resistance walls is considered to be case 3 in the previous subsection, with a value of 0.46 K · m^2/W as the closer representation of the real car cabin roof, doors and floor. The car speed is maintained to 32 km/h, the outer temperature is 43°C and the inlet temperature is 7°C.

The solar load was positioned at 180° azimuth and 45° altitude with respect to the car cabin. This implied, as shown in Figure 4.6, that the sun's direct flux is going through the windshield from the front of the cabin and at 45° from the horizontal ground. Two different cases are studied in this subsection.

- Case 5: the direct flux for the solar load was set to 1000 W/m^2 and the diffuse solar load was set to be 500 W/m^2.
- Case 6: the direct flux for the solar load was set to 500 W/m^2 and the diffuse solar load was set to be 250 W/m^2.

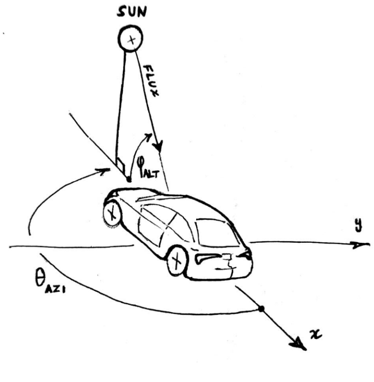

Figure 4.6: Solar load at 180º azimuth angle and 45º altitude angle

Regarding the additional conditions for the boundary surfaces, the emissivity, reflectivity, and transmissivity values must be specified. These values are listed below and shown in Figure 4.7.

- The low thermal resistance boundaries are assigned a value of transmissivity of 0.5, since the solar load radiation will partially go through the glass of the windows. An emissivity value of 0.3 and a resulting reflectivity of 0.2 are representative of a generic glass window.
- The standard and high thermal resistance boundaries, as well as the seats, are assigned a transmissivity of 0, since the solar load will not go through these boundaries. An emissivity value of 0.6 and a resulting reflectivity of 0.4 are representative of generic opaque solids.
- The inlets and outlets are assigned a transissivity of 1, letting the solar load go through these boundaries. The emissivity and reflectivity are therefore 0.

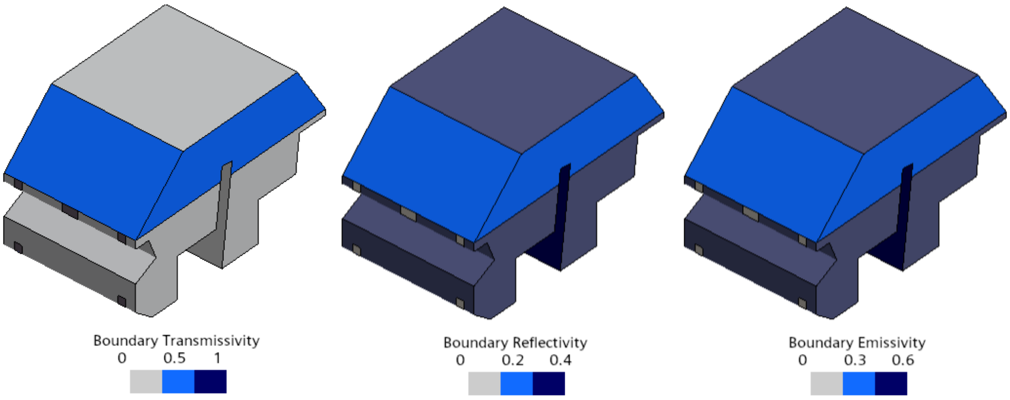

Figure 4.7: Values of reflectivity, transmissivity and emissivity for the surface boundaries of the car cabin

It has to be noted that a transmissivity of 1 was applied to the air inlets in order to prevent these from participating in the radiation heat exchange. Nevertheless, this also means that the radiation went through the air inlets and outlets, thus warming up locally some of the surfaces, which is a drawback to mention and consider.

This case study was useful to analyze the effect of heat losses in different solar load scenarios.

4.3.4 Case 7: Effect of air inlet distribution.

Similar boundary conditions as in previous Case 6 were considered, but the 68.5 g/s of air mass flow rate was applied totally to the top inlets, whereas no air mass flow rate was applied to the bottom inlets. This air mass flow rate distribution allowed for a higher amount of air mass flow to be directed at the rear seats through the central top air inlet. It also enableed an improvement of the cooling at the top areas of the car cabin.

4.3.5 Case 8: Time-step sensitivity analysis.

Similar boundary conditions as in Case 7 were applied to the present case. The main difference was that in this case study the simulation was unsteady. The temperature inside the car cabin evolved with time. A sensitivity study of the effect of the time-step size on the temperature results was performed. This was considered necessary to choose a valid time-step in order to perform the final simulations regarding the relationship between cabin average temperature and CO_2 concentration due to driver presence.

4.3.6 Case 9: Effect of variable total air mass flow rate including the driver.

Multiple steady state simulations were run with similar boundary conditions to Case 7 with two main differences. The total air mass flow rate was variated and, in addition, a driver was included to the simulation and both 1000 W/m^2 and 500 W/m^2 direct flux scenarios were studied. The intention was to analyze the relation between the average temperature in the cabin and the CO_2 concentration, leading to a global comfort conditions of air temperature and quality.

The boundary conditions applied to the driver were the following.

- The skin temperature of the human was set to 34°C.
- The nose of the driver was considered to be an additional air inlet with an air mass flow rate of 0.15 g/s, at a temperature of 37°C and with a CO_2 concentration of 40000 ppm.
- The top air inlets at the front of the cabin were specified a CO_2 concentration of 420 ppm.

Different air mass flow rates were simulated this time in order to see which was the average temperature of the cabin as well as the CO_2 concentration in each of the steady state scenarios. The simulated air mass flow rate values were 5, 10, 20, 45, 68.5, 95 and 120 g/s.

4.3.7 Case 10: Transient analysis on air temperature and quality.

Finally, specific air mass flow rates were studied in an unsteady state using the chosen time-step in Case 8, analyzing the relation in time between the average cabin temperature and the CO_2 concentration due to driver presence. Also, the 1000 W/m^2 and 500 W/m^2 direct solar load fluxes were considered.

5

Results

The summary for the cases set up can be found in Table 4.1 in subsection 4.1. Additionally, further in this chapter, a summary of the cabin boundary temperatures (Table 5.2) and of heat across boundaries (Table 5.3) can be found further in subsection 5.1.7.

5.1 Case 1: Airflow simulation without heat transfer

5.1.1 Summary of tested meshes

A summary of all the tested meshes for the mesh sensibility analysis is presented at the beginning of this chapter in Table 5.1 to improve the understanding of the followed process to the reader. All tested meshes have a common starting point, which is setting a surface cell size of 1 cm and a first prism layer height of 0.2 mm. This is defined to aim for a y+<1 in most of the boundaries of the domain together with reasonable prism layer growth ratios. Achieving y+<1 together with a reasonable growth ratio for the prism layer cells is generally accepted as a suitable method to capture the boundary layer effects in CFD [16]. Meshes 1 to 3 are aimed to achieve a coarse valid prism layer growth ratio. Meshes 3 to 3.2, use different overall maximum polyhedral cell sizes. Meshes 3.2.1 and 3.2.2, present different techniques for a volumetric control cell size refinement in the zones of considerable gradient of velocity.

Table 5.1: Tested meshes for the sensitivity analysis

Mesh	Prism layer growth ratio	no. of prism layers	Maximum polyhedral cell size [cm]	Adaptive mesh cell size [cm]	Volumetric control cell size [cm]	Total cell count [Millions]
1	1.2	13	4	NA	NA	2.7
2	1.3	10	4	NA	NA	2.2
3	1.5	8	4	NA	NA	1.9
3.1	1.5	8	2	NA	NA	2
3.2	1.5	8	1	NA	NA	4.1
3.2.1	1.5	8	4	1	NA	3.7
3.2.2	1.5	8	4	NA	1	2.7

5.1.2 Mesh sensitivity analysis

The mesh sensitivity analysis is performed using the boundary conditions and air physics described in Case 1 in the methods chapter.

According to the reasoning in subsection 5.1.1, an initial prism layer mesh sensitivity analysis is performed. The total thickness of the prism layer can be approximated before performing any numerical calculation. The total thickness must be enough to capture the boundary layer gradient effects. The boundary layer thickness can be calculated given the Reynolds number of the flow together with the characteristic length on which the velocity gradient develops.

The analysis is carried out near the central air inlet, placing a probe line near the end of the dashboard at 15 cm from the inlet (see Figure 5.1). Taking this distance as a characteristic length and calculating the air velocity according to the corresponding air mass flow rate and the inlet area, the boundary layer thickness is calculated as follows.

$$v_{inlet} = 68.5 \cdot 10^{-3} \cdot 0.8/4/1.184/(75.45 \cdot 10^{-4}) = 1.53 \quad m/s \tag{5.1}$$

$$Re = \frac{v \cdot L}{\mu} = \frac{1.53 \cdot 0.15}{1.855 \cdot 10^{-5}} = 12372 \tag{5.2}$$

$$\text{Boundary layer thickness} = 0.37 \cdot L/Re^{\frac{1}{5}} = 0.37 \cdot 0.15/12372^{\frac{1}{5}} = 0.83 \quad cm \tag{5.3}$$

A total thickness of prism layers was chosen to be 1.1 cm, which is enough to capture the boundary layer thickness. The first prism layer height is set to 0.2 mm in order to have a y+<1 on most of the domain surfaces. Nearby sharp corners and the inlets, the velocity value can be high and therefore the y+ might exceed y+<1, staying always below y+=5. Maintaining the first prism layer height and the total prism layer thickness, the effect of the growth ratio of the prism layer mesh is studied by changing the number of prism layers.

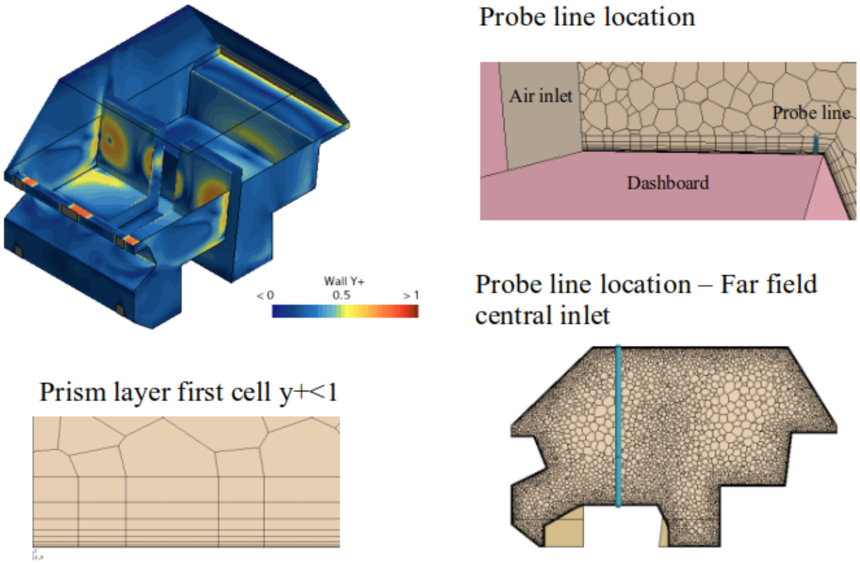

Probe line location

Probe line location – Far field central inlet

Prism layer first cell y+<1

Figure 5.1: Values of y+ below 1 in most of the car cabin surface boundaries and images regarding prism layers mesh

Three different approximate growth ratios are tested (Meshes 1 to 3). In the graphic in Figure 5.2, it can be appreciated that the gradient of velocity is properly captured by the three growth ratios. Additionally, it can be seen that the prediction for the boundary layer thickness was accurate (-1.0835 + 1.092 = 0.0085 m = 0.85 cm) and the uniform speed out of the boundary layer is 1.53 m/s.

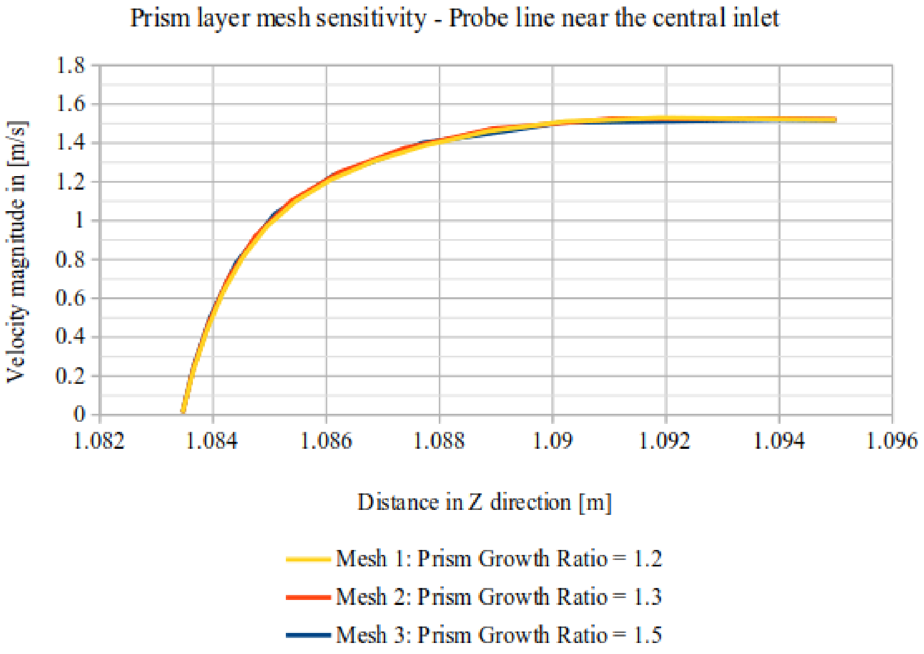

Figure 5.2: Velocity gradient captured by the prism layer mesh at a probe line 15 cm away from the central air inlet

In addition to the probe line aligned with the central air inlet and placed at the end of the dashboard, a probe line placed at the far field above the console between the seats is also analyzed. The purpose for such a study, is to see if there is any additional disturbance of the air flow at longer distances. It can be seen in the graphic below in Figure 5.3 that the velocity profile is similarly calculated in the three different meshes. The maximum velocity at the probe line is approximately 0.95 m/s in all the cases. Therefore, at this point of the mesh sensitivity analysis, the mesh with higher growth ratio is chosen since it brings lower cell count.

After the surface cell size together with the dimensions and number of prism layers is fixed, a volume mesh sensitivity analysis is carried out. Different mesh cell sizes are tested for the entire volume domain. The tried sizes were 4, 2 and 1 cm. The volume growth ratio is of 1.2 from the prism layer mesh until the target volume cell size. Analyzing the velocity profiles obtained by each of the meshes, it is interesting to see that the maximum velocity is actually sensitive to the volume cell size. As it can be observed from the graphic below in Figure 5.4, from a volume cell size of 4 cm to 1 cm, the maximum velocity changes from 0.95 m/s to 1.4 m/s. From this study, a volume cell size of 1 cm is considered to be the finest in order to properly capture the velocity gradients within the volume air domain. Nevertheless, this resolution is not necessary in the entire volume but in the zones where significant velocity gradient exists.

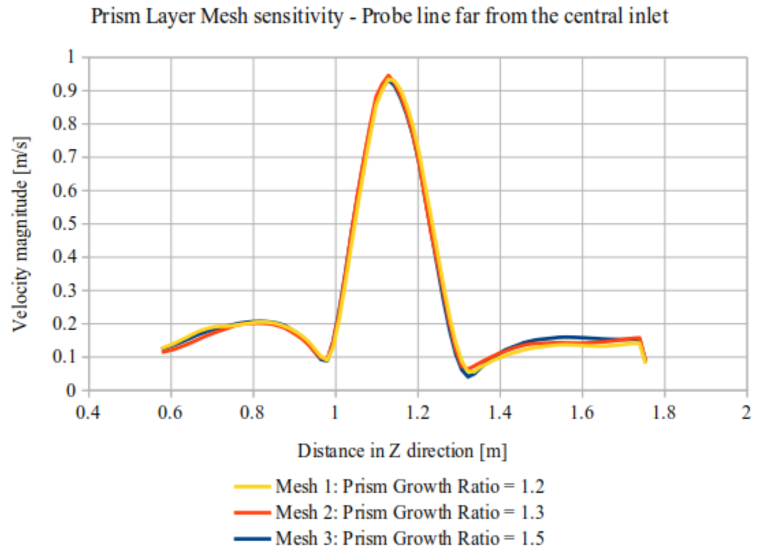

Figure 5.3: Velocity profile at a probe line far from the central air inlet

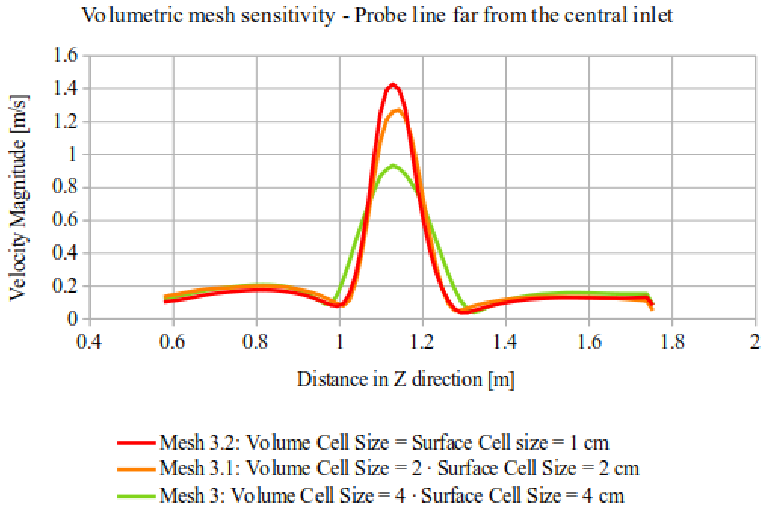

Figure 5.4: Velocity profile far from the central air inlet depending on the volume mesh cell size

Two different approaches are considered to understand which are the zones with higher velocity gradient.

A first approach is to use an adaptive mesh to iteratively reduce the volume cell size in order to reduce the cell residuals for an accurate solution. This approach refined the cells automatically at the volume zones between the inlets and the seats, as well as around the air impact zones at the seats. Nevertheless, this approach (Mesh 3.2.1) is not necessary for this application. The amount of refinement and total cell count for this approach is not easy to control. A more practical approach should be utilized.

By analyzing the velocity results, it can be seen that the main velocity gradients in the air volume domain take place between the inlets and the seats, as well as around the air impact zones at the seats. Therefore, control volumes for refinement can be manually placed around the zones of interest, specifying the 1 cm volume mesh cell size. This is the final mesh utilized for all the cases in the present research (Mesh 3.2.2 in Figure 5.5), adapting the control volumes for refinement according to each specific scenario.

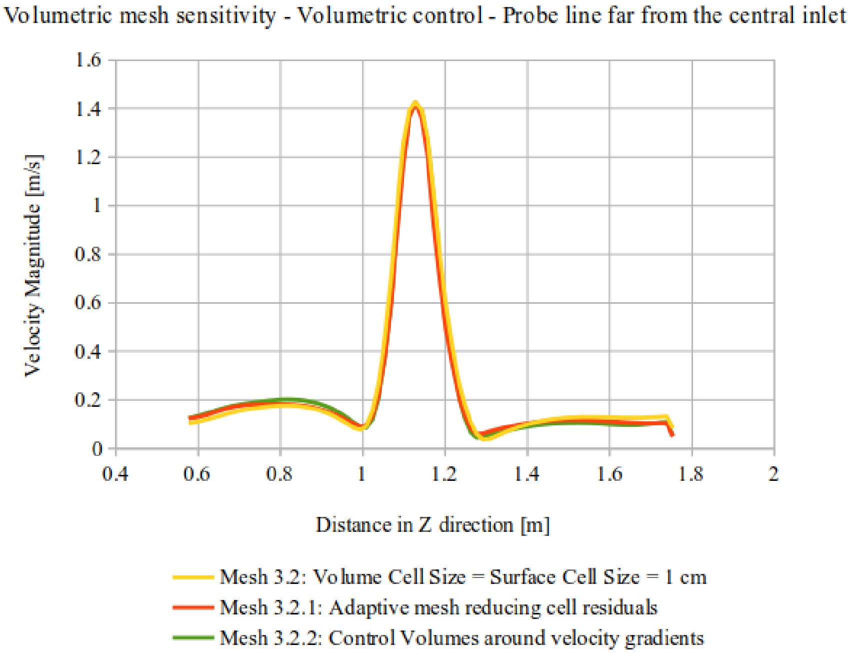

Figure 5.5: Velocity profile far from the central air inlet depending on the zones of refinement at the volume mesh

For the present case, a mesh with 2.7 million cells has been achieved and considered to capture the airflow properly in all zones within the domain. The comparison of velocity profiles obtained by line probes has not only been tested for the central air inlet but also for the remaining inlets at different distances within the air domain.

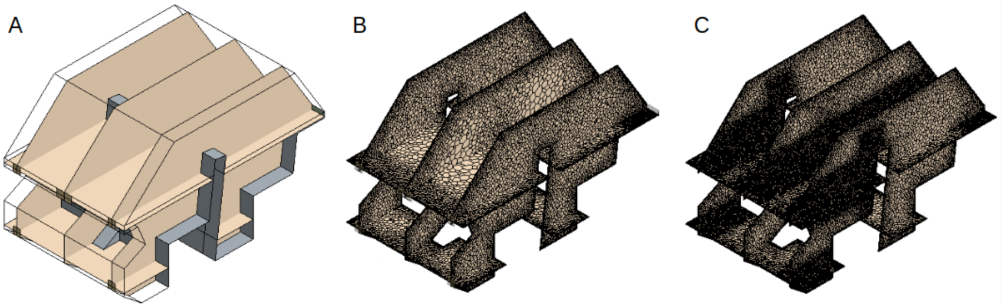

Figure 5.6: Sections of interest at air inlets (A) and evolution from Mesh 3 (B) to Mesh 3.2.2 (C) in sections of interest

5.1.3 Case 1: Airflow distribution

The resulting airflow distribution after the mesh analysis is performed can be seen in the images below.

The air velocity is 1.53 m/s at the three top air inlets and 0.75 m/s at the bottom air inlets. The two top lateral air inlets direct the air stream to the front seats. After impacting the seats, the air stream is split so one half of it is redirected to the roof and the other half is redirected to the seat base. The central air inlet directs the airflow between the two front seat to the rear seats. In this case, after the air stream impacts the rear seats, the airflow is partly directed to the rear outlet while the rest shifts towards the rear seats base. Regarding the bottom air inlets, the air streams is directly directed towards the front seats bottom. The air flow therefore recirculates nearby the front seats and underneath the dashboard.

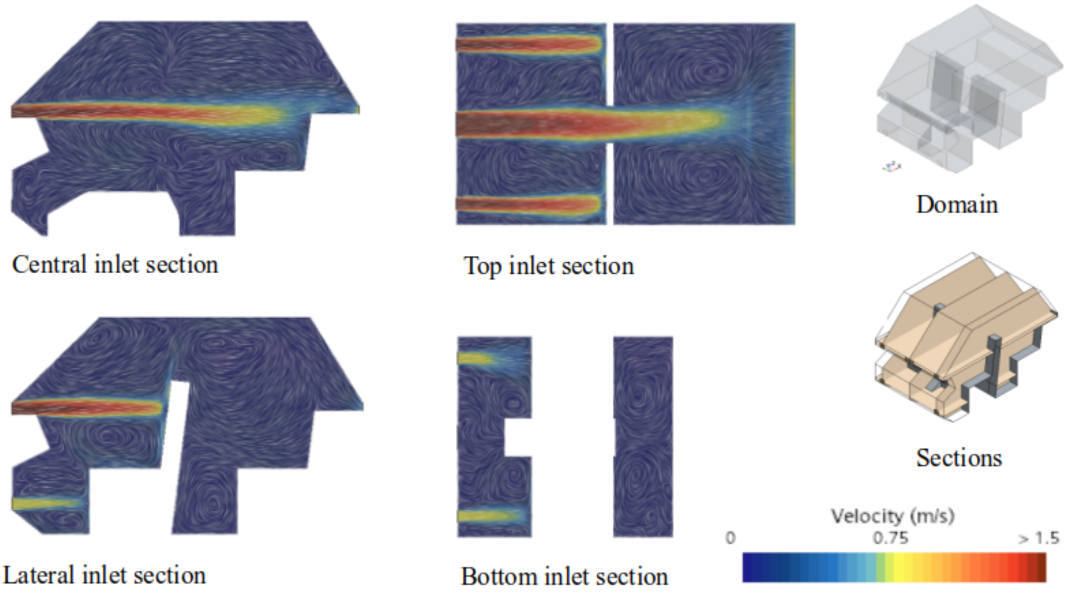
Central inlet section
Top inlet section
Domain
Sections
Lateral inlet section
Bottom inlet section

Figure 5.7: Case 1: velocity contours [m/s] and streamlines at sections along the air inlets. Domain and sections of interest at inlets within the domain at the right.

It must be pointed out that the velocity gradient within the air volume domain takes place approximately from the maximum velocity values at the air inlets to 0.5 m/s. The air velocity is below 0.5 m/s in the majority of the air volume domain, where the air forms different recirculation patterns.

5.1.4 Case 2 to 4: Effect of thermal resistance at boundaries

If a cool-down scenario is simulated, the airflow behaviour is affected by the temperature changes of the air.

In the first scenario, Case 2, all the walls but the inlets and the glasses are adiabatic. Therefore, the heat transfer between the outer 43°C air at 32 km/h and the cold 7°C air at the inlets only takes place at the windshield, lateral and rear windows.

Nevertheless, if the thermal resistance of the doors, roof and floor are gradually reduced from adiabatic to 0.46 Km^2/W and 0.06 Km^2/W, the air inside the cabin increases its steady state temperature. Therefore, the Boussinesq effects can be appreciated at first sight when visualizing the velocity contours. The cold air mainstreams fall gradually downwards, surrounded by warmer air, as the distance to the inlets increases.

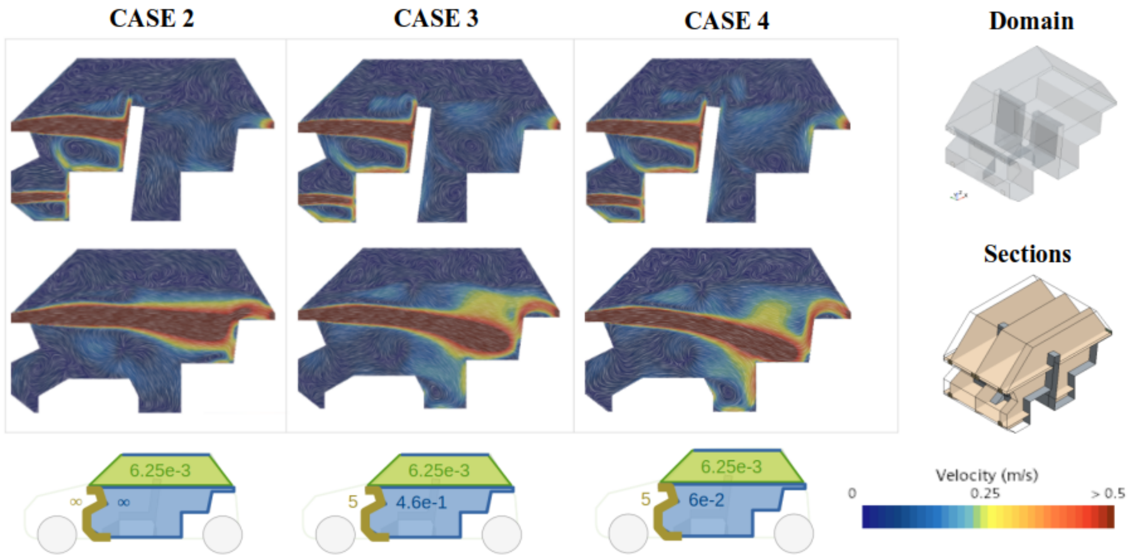

Figure 5.8: Velocity contours [m/s] and streamlines at left (top) and central (bottom) inlet sections (see the main positions at the right column). Doors, roof and floor thermal resistance values: adiabatic (left column), 0.46 Km^2/W (central column), and 0.06 Km^2/W (right column). Values of thermal resistance at the bottom row [Km^2/W]

Taking a look at the temperature contours, it can be also seen at first glance that the warm air is located upwards nearby the cabin roof, whereas the colder air remains at the bottom of the cabin . The colder area is generally located under the dashboard since the air from the bottom inlets remains in the lower front zone in which the front wall has a high thermal resistance. Regarding the volume average temperature of the cabin, it is 15.9°C with adiabatic roof, doors and floor, 17.5°C (+1.6°C) with 0.46 Km^2/W thermal resistance instead of adiabatic walls, and 19.5°C (+2°C) with the lowest thermal resistance 0.06 Km^2/W.

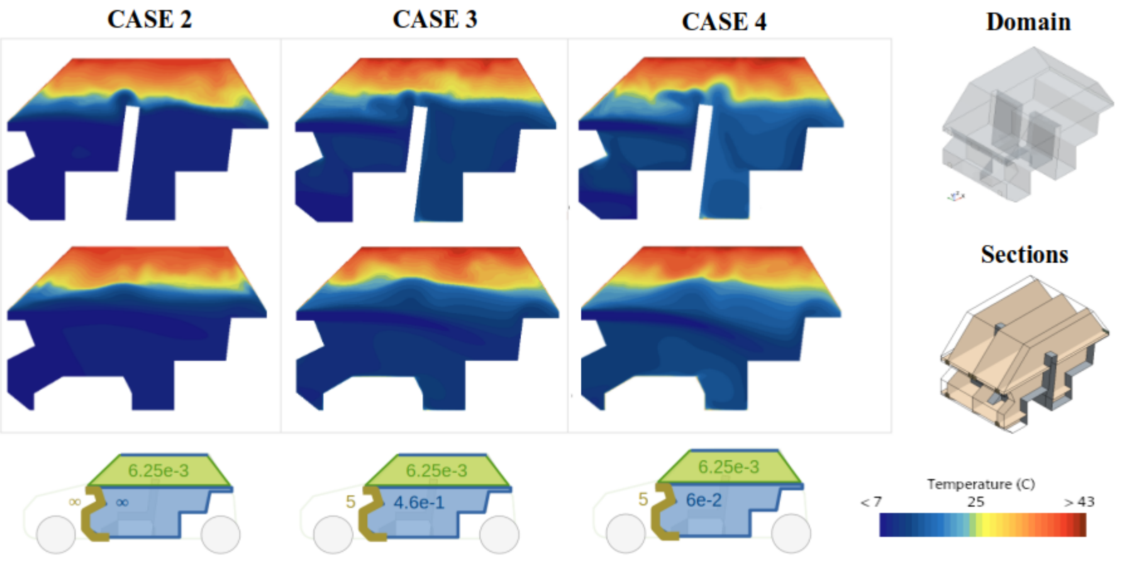

Figure 5.9: Temperature contours [°C] at left (top) and central inlet sections (bottom) (see the main positions at the right column). Doors, roof and floor thermal resistance values: adiabatic (left column), 0.46 Km^2/W (central column), and 0.06 Km^2/W (right column). Values of thermal resistance at the bottom row [Km^2/W]

Taking a look at the boundaries of the car cabin in the different cases, one can notice in more detail the mechanisms of heat transfer between the outer warm conditions and the inner cold air.

In Case 2 (Figure 5.10), the temperature at adiabatic boundaries is very near to the temperature at the air inlets, 7°C, since there is no heat exchange with the exterior and the cold air moves downwards. However, the windshield, lateral and rear windows are warm at temperatures close to the outer temperature of 43°C, increasing towards the roof height. This is caused by the convective heat transfer model applied at these boundaries. The heat transfer takes place from the outside warm air towards the inner cold air, heating it up. The amount of heat transfer is higher at the bottom of the windows, since this area is closer to the cold air jets which are the source of velocity on the air. It worth to note that the highest heat transfer takes place when the air at the boundary has an associated velocity. Observing the heat transfer coefficient inside the car cabin, it can be appreciated that these values can go up to more than 10 $W/(m^2K)$ depending on the flow characteristics at a specified y+=100.

Looking at case 3 (Figure 5.11), the mean temperature for the floor is 23 °C, the front doors is 20.7 °C, the rear doors is 22 °C and the front wall is 10.5 °C. Therefore, the heat flux at the floor is -41.2 W/m^2, the front doors is -46.2 W/m^2, the rear doors is -43.5 W/m^2 and the front wall is -6.5 W/m^2.

Looking at case 4 (Figure 5.12), the mean temperature for the floor is 35.7 °C, the front doors is 34 °C, the rear doors is 35.2 °C and the front wall is 11.5 °C. Therefore, the heat flux at the floor is -89.4 W/m^2, the front doors is -108.8 W/m^2, the rear doors is -95 W/m^2 and the front wall is -6.3 W/m^2.

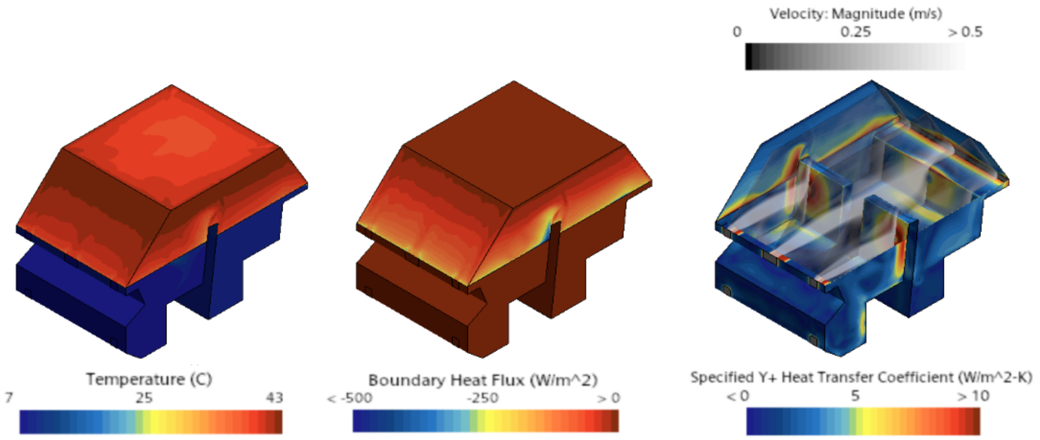

Figure 5.10: Case 2: boundary temperature [°C], heat flux [W/m^2] and heat transfer coefficient [W/(m$^2 \cdot$ K)] at y+=100 for adiabatic roof, doors and floor

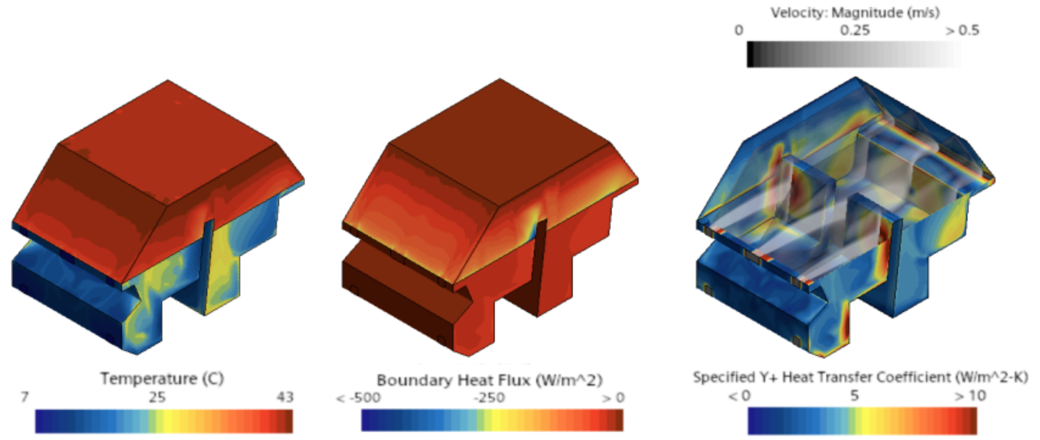

Figure 5.11: Case 3: boundary temperature [°C], heat flux [W/m^2] and heat transfer coefficient [W/(m$^2 \cdot$ K)] at y+=100 for 0.46 Km^2/W roof, doors and floor

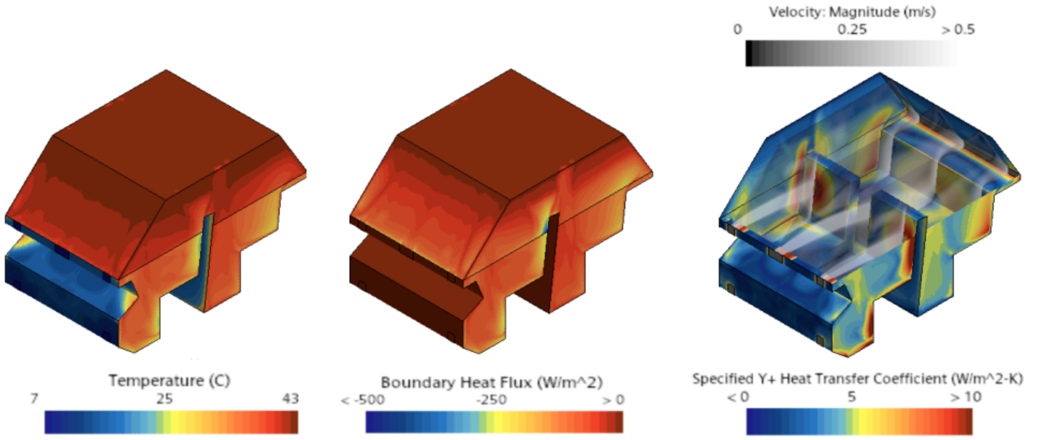

Figure 5.12: Case 4: boundary temperature [°C], heat flux [W/m^2] and heat transfer coefficient [W/(m$^2 \cdot$ K)] at y+=100 for 0.06 Km^2/W roof, doors and floor

It can be noted that the effect of the insulation has an important effect on the heat transfer scenario. The lower the insulation value, the higher the temperature obtained at the boundaries. While the increase of temperatures from case 2 to case 4 at the boundaries is large (more than 10°C from case to case), the average temperature of the air within the car cabin increases in lower values (around 1.5°C and 2°C from case to case).
A bars graphic (Figure 5.13) below shows the heat across boundaries from each of the car cabin boundaries. In addition to the last statements, it can be observed that the heat transfer at the roof is minimal since the warm air at the top of the cabin is near to 43°C. In the case of the windows, the heat transfer is similar between cases since the thermal resistance and convection properties are the same.

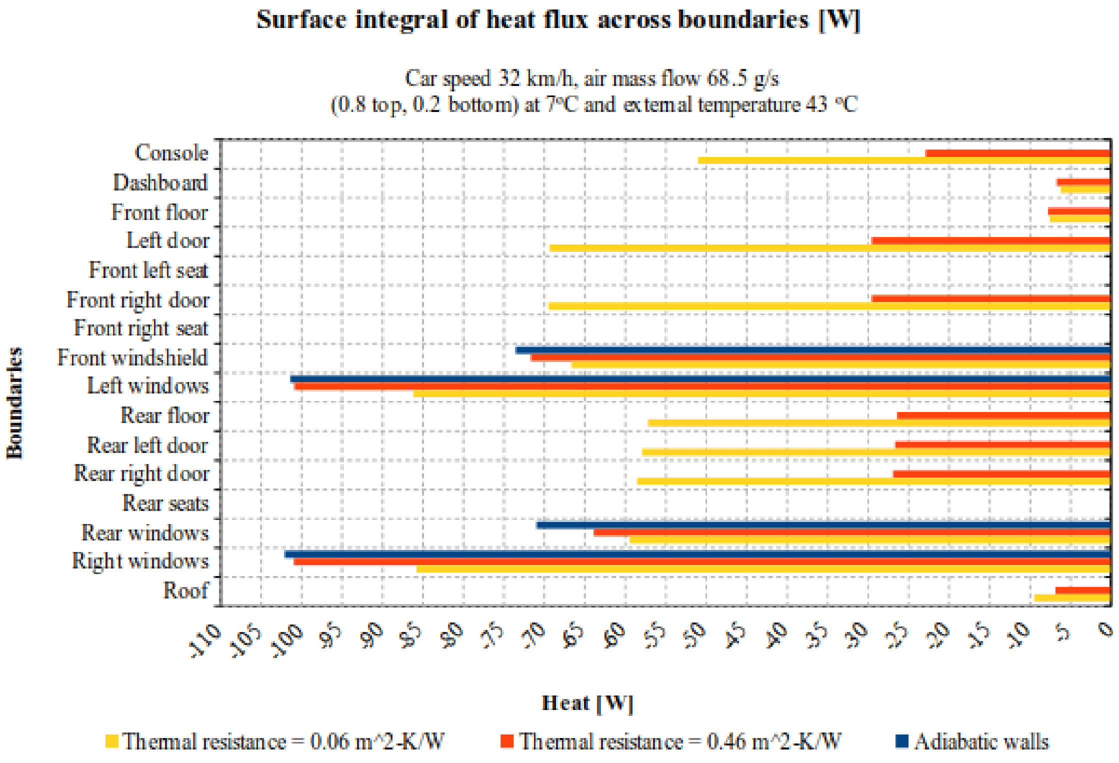

Figure 5.13: Heat [W] through the boundaries at different insulation levels

Analyzing the graphic, it can be said that the highest absolute value of heat flux takes place at the windshield and windows. Nevertheless, the thermal resistance of the windows was not modified. Interesting is that the boundaries which need better insulation in a cool-down scenario, are the doors and floor since they are located in a low position, where the interior cold air remains and contrasts with the high outer temperature. Regarding the front of the cabin, it usually presents a high thermal resistance and requires less attention.

Regarding the roof, there is a low heat flux through it since the warm air inside the cabin remains in the upper position and there is a lower temperature difference with the exterior. Therefore, the appropriate level of insulation for the roof should consider a warm-up scenario.

Finally, the seats reach a specific temperature at a steady state, and no heat exchange takes place at their boundaries.

5.1.5 Case 5 and 6: Effect of solar load

In this section, a similar analysis is carried out to study the effect of solar load. The studied scenarios are Case 5 with 500 W/m^2 solar direct flux and 250 W/m^2 solar diffuse flux and Case 6 with solar direct flux 1000 W/m^2 and solar diffuse flux with 500W/m^2. The selected standard thermal resistance for the walls is 0.46 Km^2/W for roof, doors and floor. The high thermal resistance wall is 5 Km^2/W for the front wall, which includes the front floor and the dashboard, and adiabatic for the seats.

Observing the resulting airflow in Figure 5.14, it can be noticed that the effect of the cold air jets falling downwards is increased if compared with the cases with no solar load. This is caused because the solar loads increase the temperature of the boundaries of the car cabin, which is transferred by convection to the air surrounding the cold air jets. Therefore, the Buoyancy effect is magnified.

Taking a look to the temperature contours in Figure 5.15, it can be seen that the general value of air temperature is increased. The average volume temperature for the lowest solar load case is 23.2 °C, whereas it is 27 °C for the maximum solar load case. Therefore, there is an increase of average air temperature of +5.7 °C from Case 3 to Case 5 (from no solar load to the lowest solar load scenario) and +3.8 °C from Case 5 to Case 6 (from the lowest solar load to the maximum solar load scenario).

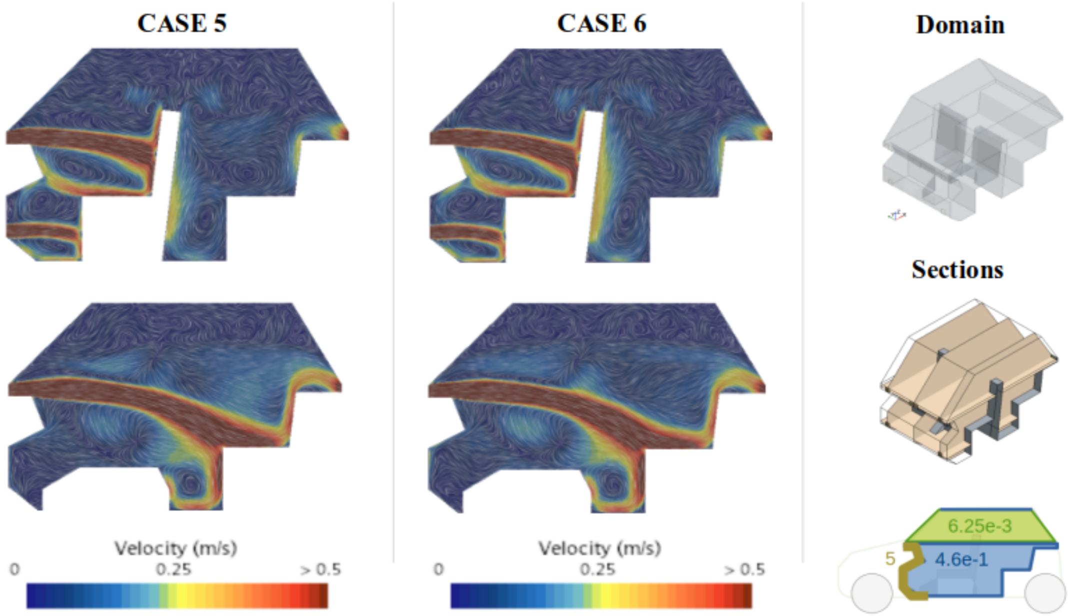

Figure 5.14: Velocity contours [m/s] and streamlines at left (top) and central (bottom) inlet sections with doors, roof and floor thermal resistance 0.46 Km^2/W. Direct solar flux 500 W/m^2 (Case 5) and 1000 W/m^2 (Case 6). Thermal resistance values [Km^2/W] at bottom right corner. Domain and sections of interest at inlets to the right.

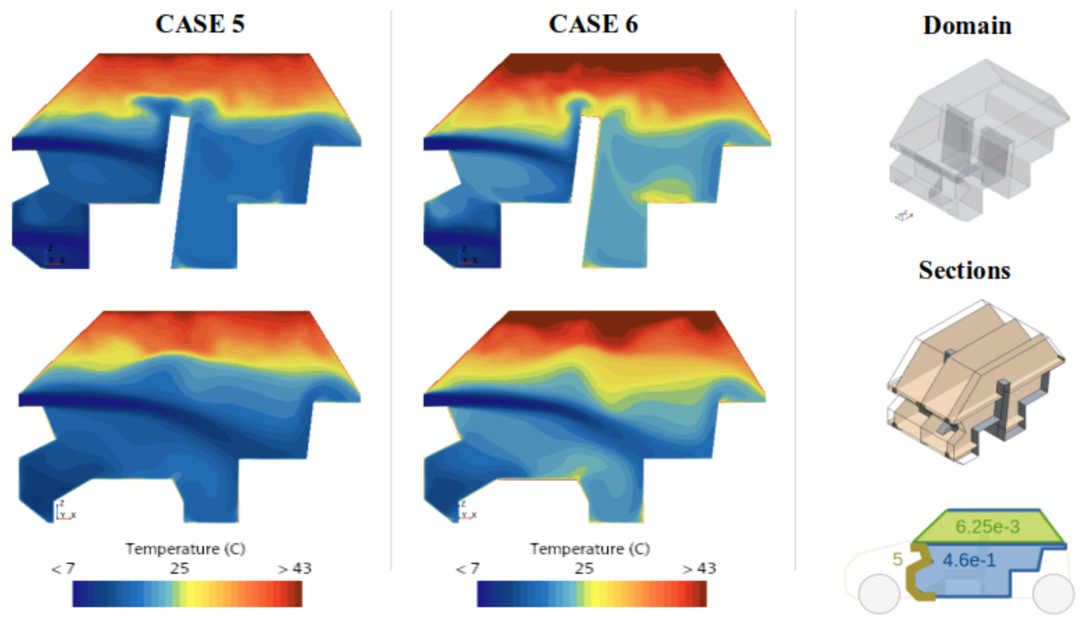

Figure 5.15: Temperature [°C] contours at left (top) and central (bottom) inlet sections with doors, roof and floor thermal resistance 0.46 Km^2/W. Direct solar flux 500 W/m^2 (Case 5) and 1000 W/m^2 (Case 6). Thermal resistance values [Km^2/W] at bottom right corner. Domain and sections of interest at inlets to the right.

Taking a look at the car cabin boundaries, it can be perceived that the average temperatures have also augmented.

For Case 5 (Figure 5.16), the mean temperature for the floor is 29.5 °C, the front doors is 30 °C, the rear doors is 31.5 °C and the front wall is 21.8 °C. Therefore, the heat loss at the floor is -28 W/m^2, the front doors is -27 W/m^2, the rear doors is -23.8 W/m^2 and the front wall is -4.2 W/m^2.

For Case 6 (Figure 5.17), the mean temperature for the floor is 35.3 °C, the front doors is 36.7 °C, the rear doors is 37.4 °C and the front wall is 26.8 °C. Therefore, the heat loss at the floor is -16.1 W/m^2, the front doors is -13 W/m^2, the rear doors is -11.2 W/m^2 and the front wall is -3.2 W/m^2.

It can be noticed that for the 1000 W/m^2 direct solar load case, the maximum temperature nearby the roof is around 60°C. To this point of the research, with all the main necessary conditions to model a realistic case, the obtained temperature inside the car cabin is far from comfortable. This is an expected result, since the air mass flow rate taken from literature is suitable for a cool-down scenario with ambient temperature of 30°C and 800 W/m^2 solar radiation flux.

As the numbers above show, there is a significant increase of temperature at the car cabin boundaries due to the incident solar radiation. The radiation heats up the surfaces directly while the fluid cool them down. The air within the cabin increases its temperature as well by convection and conduction effect on the walls. It is interesting to compare the windshield and windows heat flux since at 500 W/m^2 (Fig 5.16) there is a significant amount of cold air above the inlets, generating most of heat flux inwards to the cabin.

In contrast, at 1000 W/m^2 (Fig 5.17) the air above the top air inlets is mostly warm, generating most of heat flux outwards of the cabin.

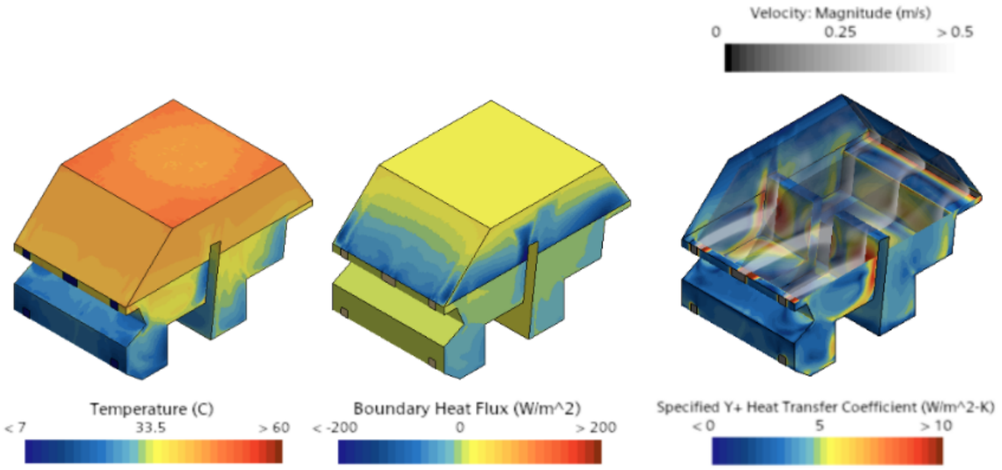

Figure 5.16: Case 5: car cabin boundary temperature [°C], heat flux [W/m^2] and heat transfer coefficient[W/(m$^2 \cdot$ K)] for 0.46 Km^2/W roof, doors and floor and 500 W/m^2 direct 250 W/m^2 diffuse solar load.

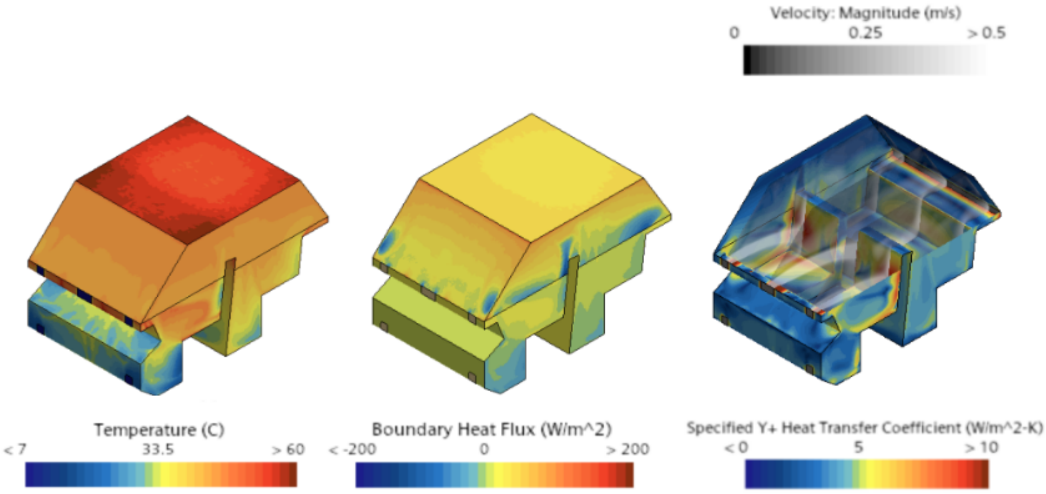

Figure 5.17: Case 6: car cabin boundary temperature [°C], heat flux [W/m^2] and heat transfer coefficient[W/(m$^2 \cdot$ K)] for 0.46 Km^2/W roof, doors and floor and 1000 W/m^2 direct 500 W/m^2 diffuse solar load.

In the Figure 5.18, it can be observed that the the heat is transferred from the exterior to the interior of the car cabin in Case 5, while it turns into heat transferred from inside the cabin to the exterior in Case 6. The explanation for this is that the radiation of the solar load directed to the windows and windshield is mostly transmitted at the glass materials without warming them by radiation. The average temperature of the windows and windshield is also nearby 43°C in both solar load scenarios. The inner air nearby the windows and windshield increases significantly, producing the described effect in heat flux.

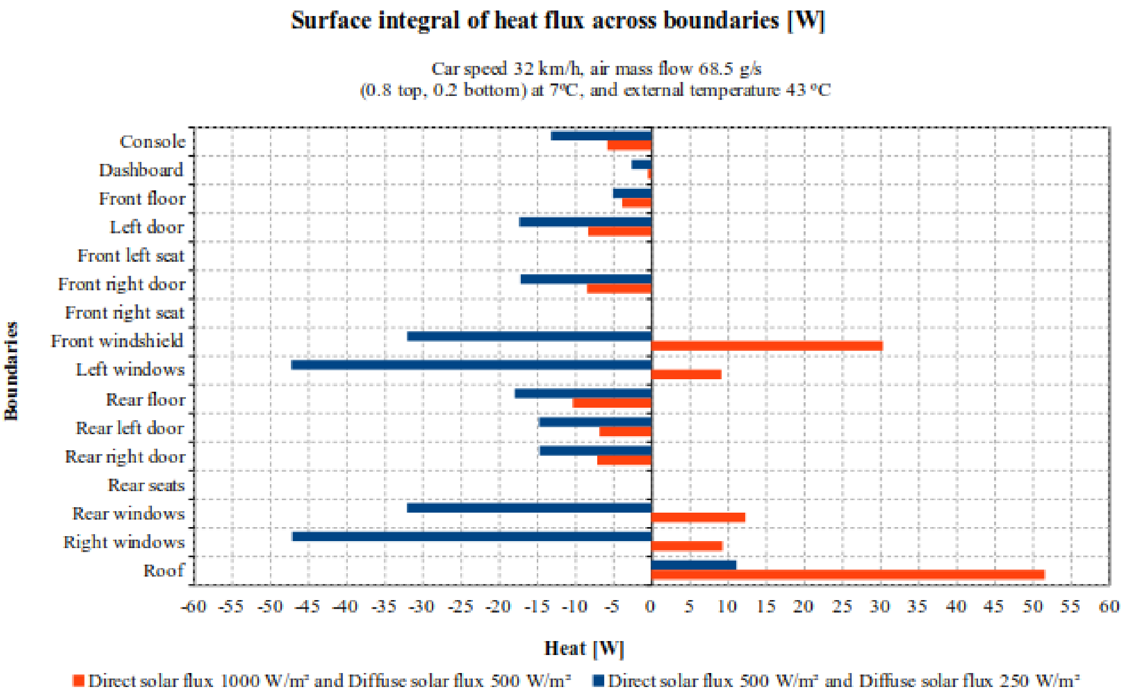

Figure 5.18: Heat [W] through the car cabin boundaries for Case 5 and 6.

5.1.6 Case 7: Effect of air inlet distribution

After analyzing Case 5 and 6, at first glance it can be seen that the front feet areas are the colder zones in the car cabin, whereas the top area nearby the roof are the warmest.

Taking the literature as a reference, in a summer HVAC program scenario, only a proportion of 0.05 of the total air mass flow is directed to the feet zone, while 0.15 is directed to the rear seats.

After observing the results in the present study, it is intuitive that a different air mass flow distribution may lead to better air temperature distribution within the car cabin. Maintaining the air inlets in the same position, a larger amount of airflow can be directed towards the roof and the rear seats by applying the entire air mass flow to the top air inlets and canceling the bottom air inlets. The effects of such a change in airflow distribution is studied.

This time, for Case 7, the air inlet velocity is 1.92 m/s.

$$v_{inlet} = 68.5 \cdot 10^{-3} \cdot 1/4/1.184/(75.45 \cdot 10^{-4}) = 1.92 \quad m/s \tag{5.4}$$

Looking at the temperature results in Figure 5.19, it can be seen that the air temperature above the air jets is now reduced as forecasted if compared with the initial air inlet distribution. In addition, the air at the front bottom is higher as the bottom cooling has been cancelled.

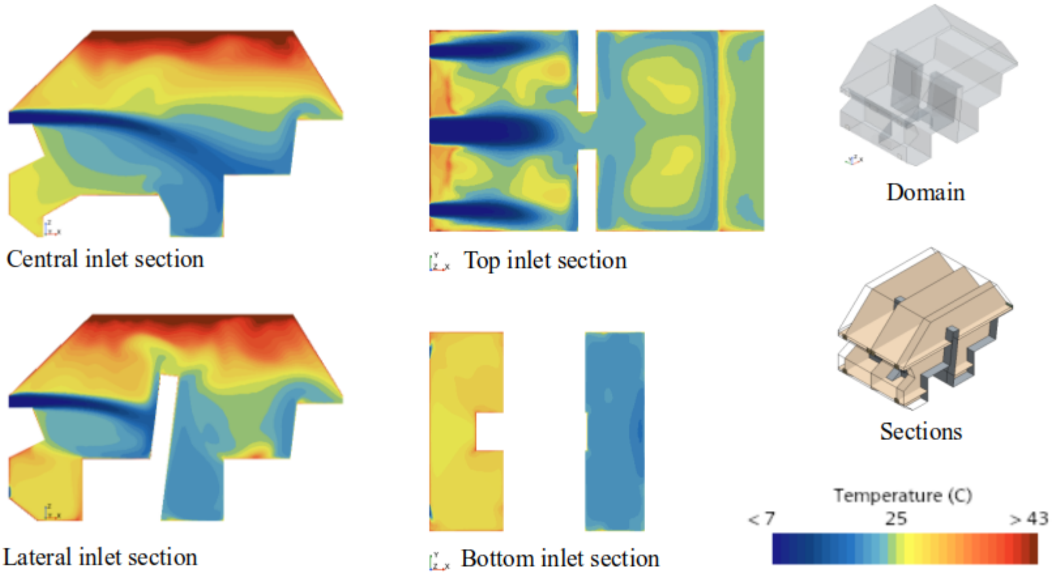

Figure 5.19: Case 7: contours of temperature [°C] at the main air inlet sections.

A deeper analysis on the heat transfer by radiation and the heat transfer coefficient within the cabin is offered in this case (Figure 5.20). Observing the results in the figure below, if the interior of the car cabin is observed, one can notice that the surfaces maximum temperatures reach temperatures up to 83°C.

The highest temperature takes place at the top of the dashboard, nearby the front windshield. This high temperature is caused by the effect of solar load on the surface, which in addition does not receive a proper cooling from the air jets. Also, the front seats present a high temperature with a local maximum temperature of 70°C. This can be explained as they receive the cooling from the lateral air jets, taking the minimum seat temperature to 34°C at the impact zone.

It has to be noted that the Boussinesq approximation may produce significant local errors at these high temperature surfaces. A parallel study considering the ideal gas equation solving for density variations could lead to different results. This was not tested by the project time constrain.

At the rear seats, the temperature at the boundaries is lower. The direct solar flux received by the rear seats only reaches between the two front seats ending up at the lower feet zone. Therefore, at that zone the maximum temperature is 53°C whereas the minimum temperature is 28°C at the points where the air jet impacts the rear seats.

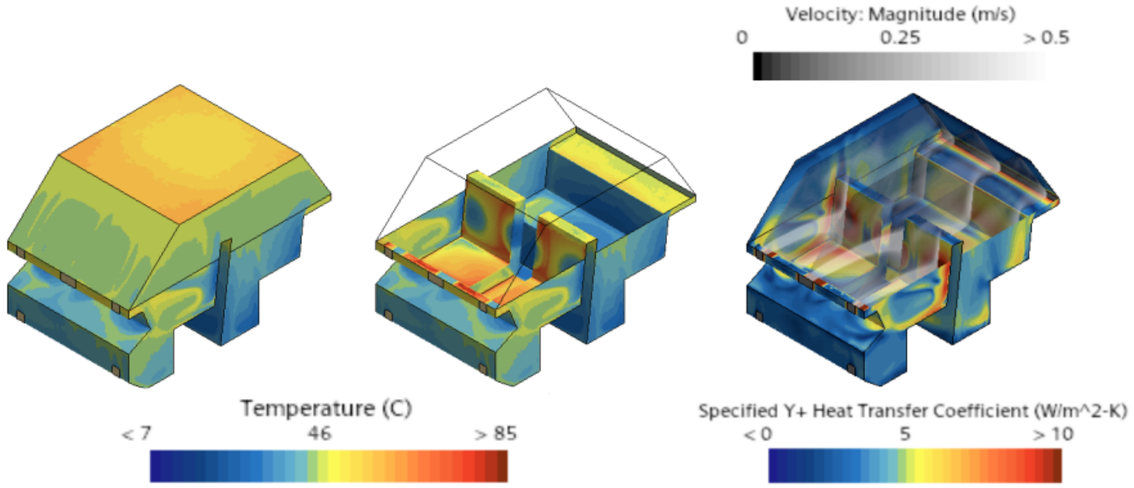

Figure 5.20: Case 7: temperature contours [°C] and heat transfer coefficient [W/(m^{2}K)] at boundaries

It can also be pointed that the zones of minimum temperatures on the boundaries are related to low air jet temperatures impacting these surfaces, and bottom zones where the cold air remains as it moves downwards. At the impact zone of the air jet, the air is at its coldest point on the surface. After the impact, the air accelerates on the seat surfaces, making the heat transfer coefficient the maximum after the values on the dashboard for the inlet air. After that, the air stays attached to the surface of the seats at velocities around 0.5 m/s until the detachment at sharp geometries. As the attached air advances, its temperature increases since it continues to absorb heat from the surfaces.

Out of the impact zone of the air jets, the velocity of the attached air is important for the convection heat transfer mechanism. Higher speeds of air would lead to higher rate of cold air renewal, improving the capability of transferring heat from the warm surfaces to the cold air.

Taking a look at the radiation results in Figure 5.21, it can be noticed in the figure below that the surfaces which have the highest irradiation are the front seats, the console, and the lower zone of the rear seats which falls between the two front seats. This is because the boundary condition set for the direct solar flux is specified to be 180º azimuth, which positions the sun in front of the car cabin, and 45º in altitude, which directs the direct solar flux at 45º from the horizontal plane. Therefore, the direct solar load reaches the interior going through the windshield perpendicularly. The rest of the surfaces receive the diffuse solar load, as well as the radiation coming from the surrounding surfaces. This explains therefore the low temperatures at the rear seats, as the direct solar load does not fully reach the rear zone.

Finally, its interesting to see how the boundary heat flux has changed in this case. Since the air mass flow is applied totally at the top inlets, the cold air jets reduce the air temperature at the upper areas of the car cabin. Nevertheless, this also implies cold air streams at higher velocities nearby the windshield and windows. It can be notice therefore that there is an increased flux of heat from the ambient towards the interior of the cabin through the the windshield and the windows.

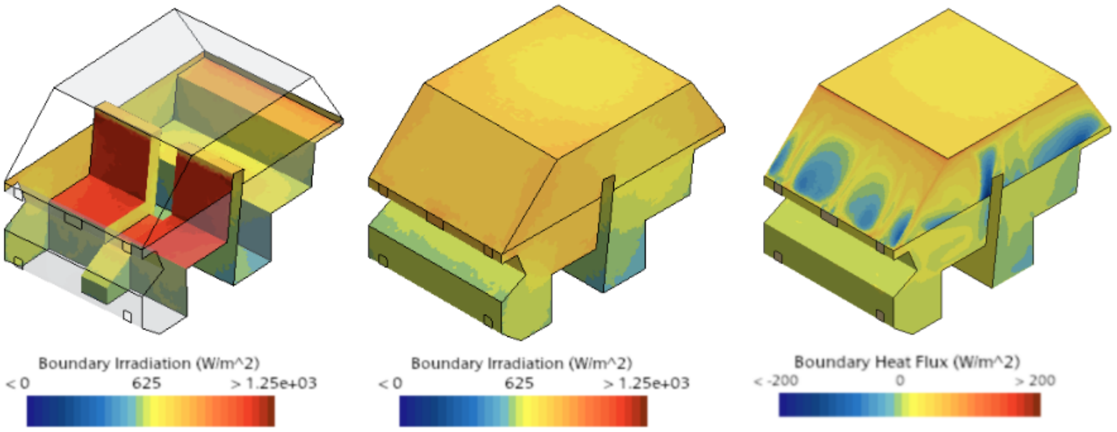

Figure 5.21: Case 7: boundary irradiation [W/m^2] and boundary heat flux [W/m^2] at car cabin boundaries.

As shown in Figure 5.22, in order to locally evaluate the change in temperature of the interior air, a series of point probes are generated in characteristic zones for the passengers within the car cabin, including head, knees and feet.

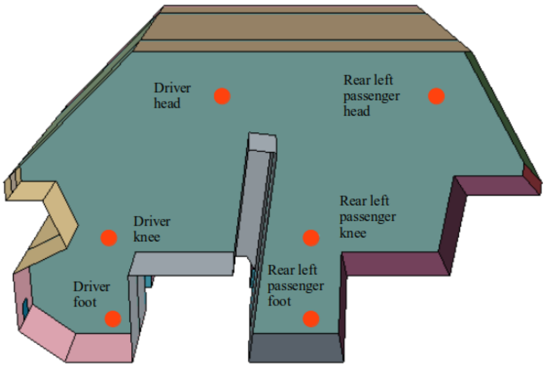

Figure 5.22: Representation of probe points at characteristic passenger areas.

The temperatures at the probe points are displayed in Figure 5.23. From this, the potential improvement can be measured more accurately. Cancelling the airflow at the bottom inlets to concentrate it to the top has increased the temperature at the feet by 10°C. In return, the air temperature at knees and head of the front passengers has decreased up to 5°C in most of the probe points. In Figure 5.24, it can be seen that the heat through the windows and front windshield has increased from the ambient towards the cabin. The bottom front boundaries, since they are not directly cooled, present almost no heat transfer towards the cabin. There is also a noticeable heat increase from the exterior towards the interior through the rear floor and doors, as the air mass flow rate at the central inlet has also increased. All this extra heat towards the cabin produced by the new air distribution has a value of -28.1 W, raising the average temperature of the air from 27°C to 28.2°C if compared to the case in which all the air inlets are used.

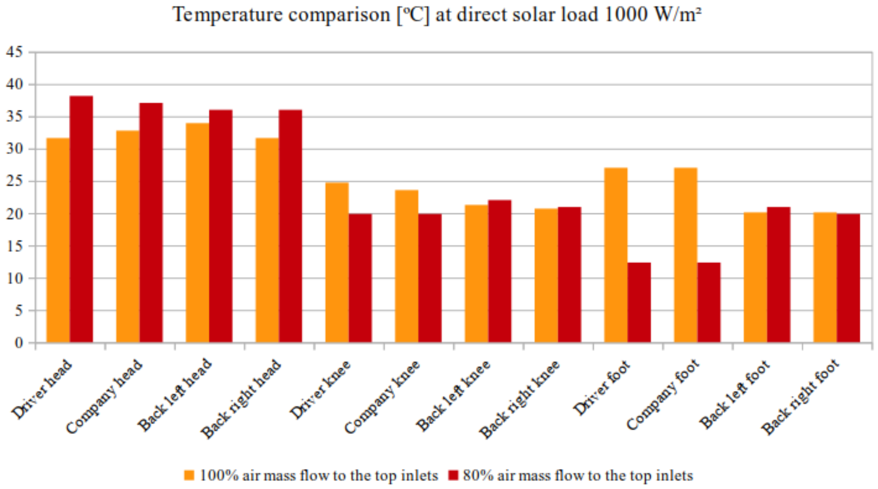

Figure 5.23: Temperature [°C] at probe points at different air mass flow distributions at inlets.

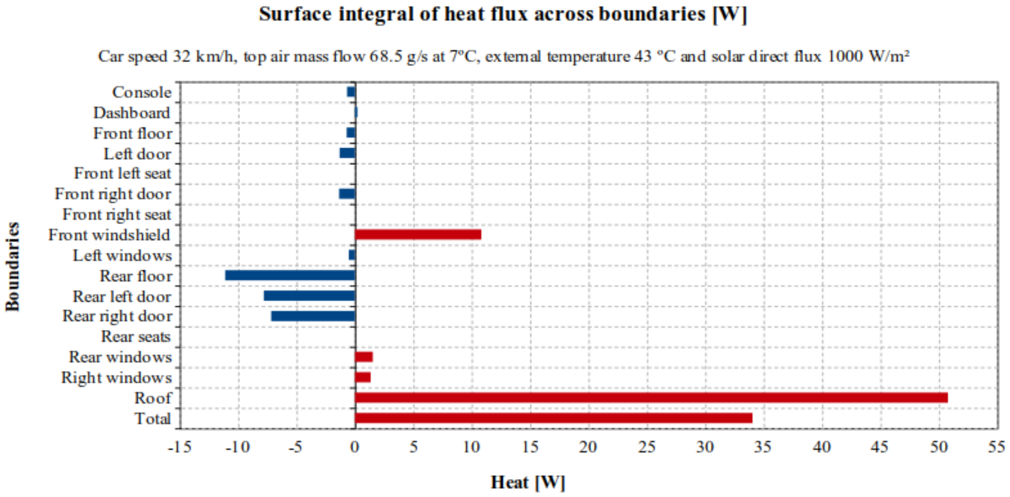

Figure 5.24: Heat through the boundaries [W] of the car cabin for Case 7.

5.1.7 Case 2 to 7: Summary of temperature and heat across the cabin boundaries

Table 5.2: Case 2 to 7: surface average temperature [°C] at cabin boundaries

Temperature [°C]	Console	Dashboard	Front floor	Front left door	Front left seat	Front right door	Front right seat	Front wind-shield	Left win-dows	Rear floor	Rear left door	Rear right door	Rear seats	Rear window	Right win-dows	Roof
Case 2	7.6	7.5	7	7.5	8.5	7.5	8.5	41.3	40.1	8.4	8.5	8.5	8.6	41	40.4	39.4
Case 3	21.8	13	10.5	20.7	11.8	20.7	11.7	41.3	40.5	23.2	22.2	22	11.3	41.2	40.5	41.4
Case 4	35	15.4	11.4	34.1	14.3	34.1	14.3	41.5	40.8	35.7	35.3	35.3	13.6	41.3	40.9	42.6
Case 5	30.8	31.4	21.8	30	31	30	31	42.3	42	29.5	31.5	31.5	29	42.1	41.8	45.6
Case 6	37.7	41	26.8	36.8	41.6	36.6	41.4	43.7	43.2	35.3	37.7	37.5	37.3	42.2	43.2	54.9
Case 7	42	44	40	42	44	42	44	43	43	34.6	37	37	37	43	1.3	54.7

Table 5.3: Case 2 to 7: surface heat flux integral [W] at cabin boundaries

Heat [W]	Console	Dashboard	Front floor	Front left door	Front left seat	Front right door	Front right seat	Front windshield	Left windows	Rear floor	Rear left door	Rear right door	Rear seats	Rear window	Right windows	Roof	Total
Case 2	0	0	0	0	0	0	0	-73.4	-101.3	0	0	0	0	-70.8	-102	0	-347.5
Case 3	-22.8	-6.6	-7.7	-29.5	0	-29.5	0	-71.6	-100.8	-26.3	-26.6	-26.8	0	-63.8	-100.8	-6.8	-519.4
Case 4	-50.9	-6.1	-7.4	-69.3	0	-69.4	0	-66.5	-86.1	-57.1	-57.8	-58.4	0	-59.4	-85.7	-9.3	-683.5
Case 5	-13.1	-2.66	-5	-17.3	0	-17.1	0	-32	-47.2	-17.9	-14.7	-14.6	0	-32	-47	11.2	-249.2
Case 6	-5.7	-0.43	-38.1	-8.2	0	-8.41	0	30.4	9.2	-10.3	-6.8	-7.1	0	12.3	9.3	51.6	62.3
Case 7	-67.1	-0.2	-0.7	-1.3	0	-1.4	0	10.8	-0.52	-11.1	-7.8	-7.2	0	1.5	43	50.7	34

5.1.8 Case 8: Time-step sensitivity analysis

For a better understanding of the cooling down scenario, a transient simulation is necessary. In this subsection the effect in time-step selection for a transient simulation is presented.

Similar conditions to Case 7 were applied for Case 8, changing the study from steady state to an unsteady simulation.

The evolution of temperature in all the probe points was tracked in time. The starting considered temperature is 43°C. A transient decrease of the temperature in all points was observed, until reaching a steady state in which the temperatur oscillates around an average constant value. The legend for the probe points of interest can be seen in Figure 2.25.

Figure 5.25: Monitor on probe points which tracked the temperature [°C] with respect to time [s]. Legend for the transient graphs in the next page.

The different time-steps which have been tried are from coarser to finer 1, 0.5 and 0.1 seconds. It can be observed that the main difference between the graphs (Figure 5.26 to 5.28) takes place at the first 40 seconds of the simulation, in which a time-step of 0.1s is necessary to properly define the evolution in temperature. Nevertheless, after these 40 seconds, the evolution of temperature is similar for all the time-steps, reaching a steady-state after approximately 200 seconds. Since the interest of the transient simulations is not to understand accurately the first seconds but the overall evolution until the steady-state, a time-step of 1 second was considered accurate enough to perform an analysis on the transient behaviour of temperature and CO_2 concentration for the coming cases.

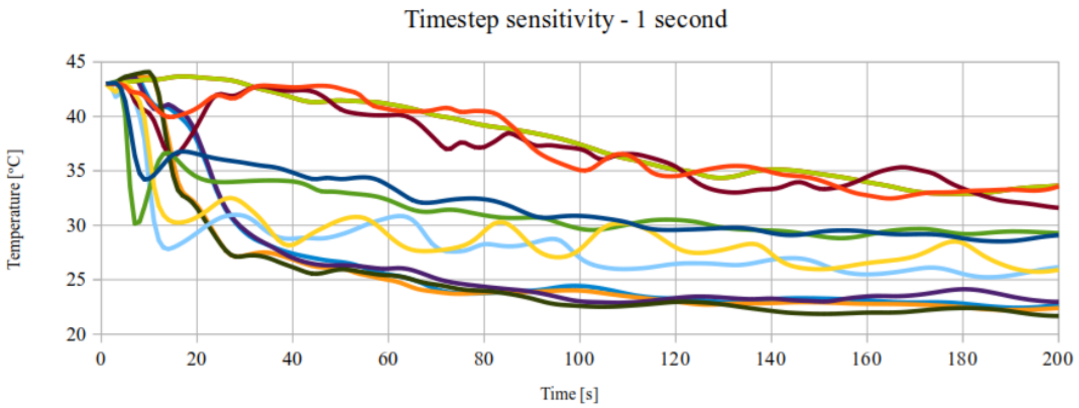

Figure 5.26: Transient temperature [Cº] at probe points with 1s time-step

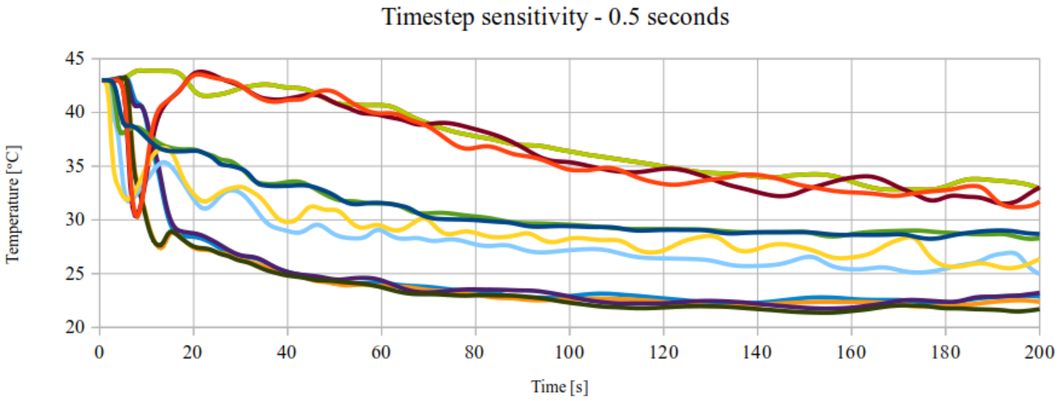

Figure 5.27: Transient temperature [Cº] at probe points with 0.5s time-step

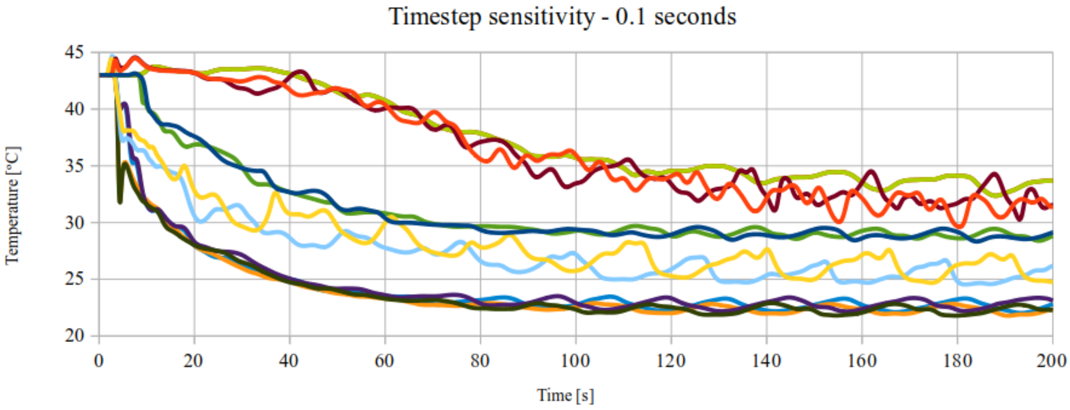

Figure 5.28: Transient temperature [Cº] at probe points with 0.1s time-step

5.1.9 Case 9: Effect of variable total air mass flow rate including the driver

After the validation of the required transient time-step resolution in Case 8, the relation between thermal comfort, air quality and energy consumption is presented in the present Case 9.

To perform such a study, a mannequin was added as a driver and several steady-state cases for different air mass flow rates were simulated, representing the steady volume average temperature and CO_2 concentration. This was done for the two cases of solar load, direct solar load 500 W/m^2 and 1000 W/m^2.

The considered range for thermal comfort comprises average cabin temperatures from 18°C to 26°C. Temperatures around 18°C within the range are considered to properly cool down the car cabin at the expense of excessive energy consumption from the HVAC unit, whereas temperatures around 26°C is considered the borderline of proper cool down for the cabin, in which the energy consumption is optimal at the expense of lower thermal comfort for the passengers. Therefore, the optimal point of thermal comfort considering a reasonable energy consumption is at 22°C.
Regarding the CO_2 concentration, levels above 1000 ppm are associated with poor air quality and drowsiness. Low air mass flow rates lead not only to thermal discomfort, but also to poor air quality. The effect CO_2 concentration increases with the presence of more passengers and has to be taken into consideration.

Below, two graphs are presented for direct solar fluxes of 500 W/m^2 (Figure 5.29) and 1000 W/m^2 (Figure 5.30).

For the lowest solar load, it can be seen that the range of air mass flow to reach thermal comfort ranges from 60 g/s to 120 g/s, reaching the lowest average temperature of 20°C. The CO_2 levels for this range of air mass flow rate are below the 1000 ppm limit, around 525 and 477 ppm.

For the highest solar load, it can be seen that the range of air mass flow to reach thermal comfort ranges from 85 g/s to 120 g/s, reaching the lowest average temperature of 23°C. The CO_2 levels for this range of air mass flow rate are below the 1000 ppm limit, around 500 and 460 ppm.

It has to be considered though that for more passengers, the air quality requirement may not be met. The same can be said for the thermal comfort, as the average temperature of the air also increases with passengers. In this case, from Case 7 to Case 9, if comparing the simulations at 1000 W/m^2 without and with driver, the average temperature of the air increases from 28.2°C to 28.4°C.

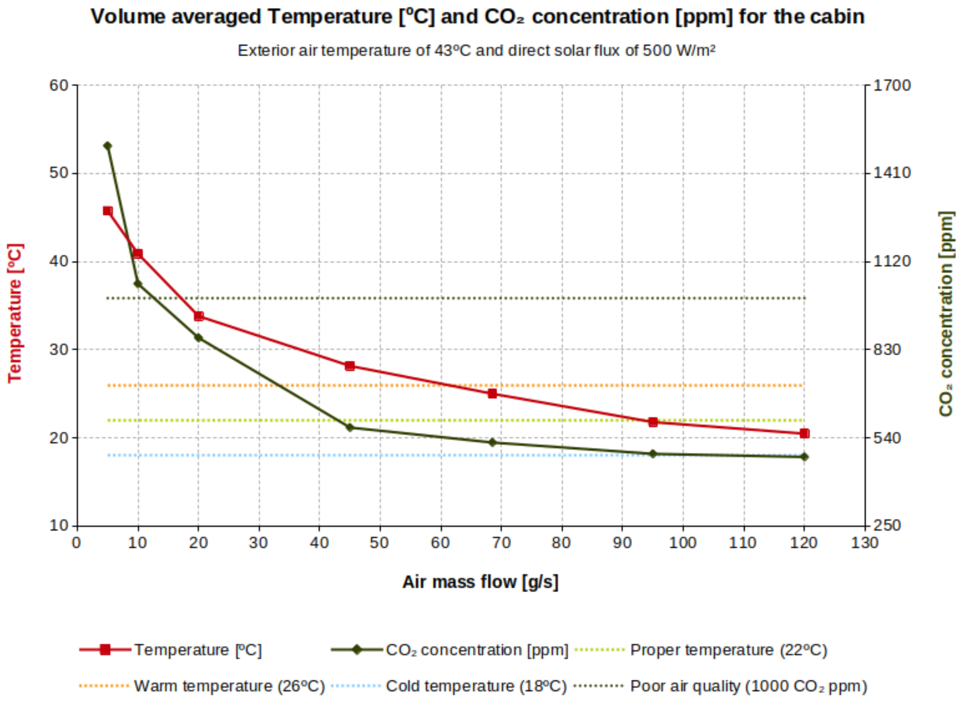

Figure 5.29: Volumetric average temperature [°C] and CO_2 concentration [ppm] at 500 W/m^2 for different total air mass flow rate values [g/s]

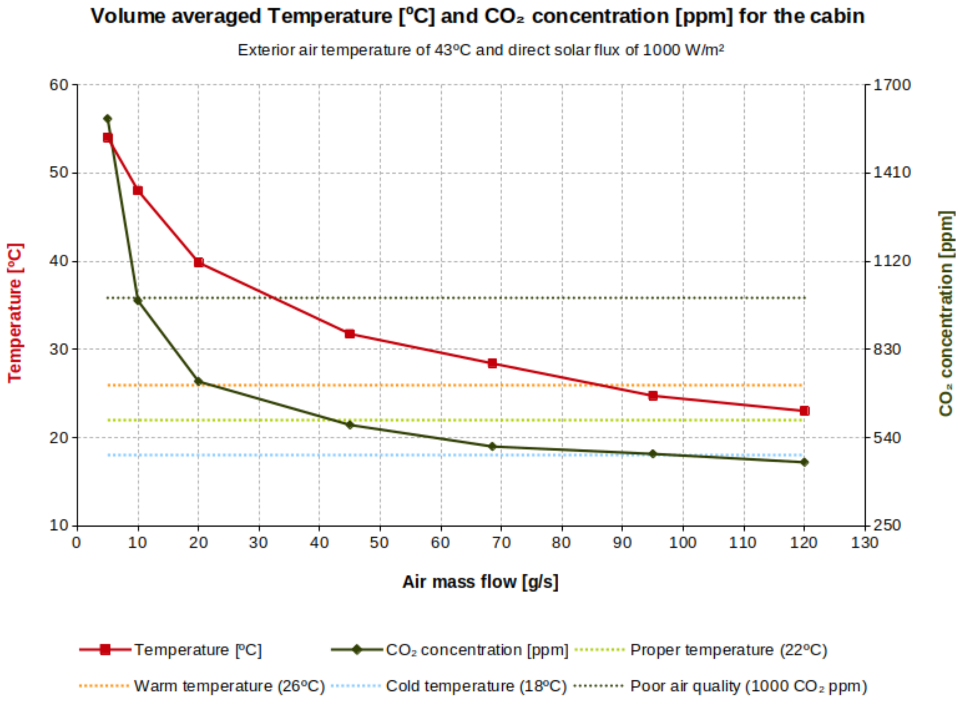

Figure 5.30: Volumetric average temperature [°C] and CO_2 concentration [ppm] at 1000 W/m^2 for different total air mass flow rate values [g/s]

It is interesting to quantify the amount of required power for the HVAC unit to reach thermal comfort and air quality (Figure 5.31).

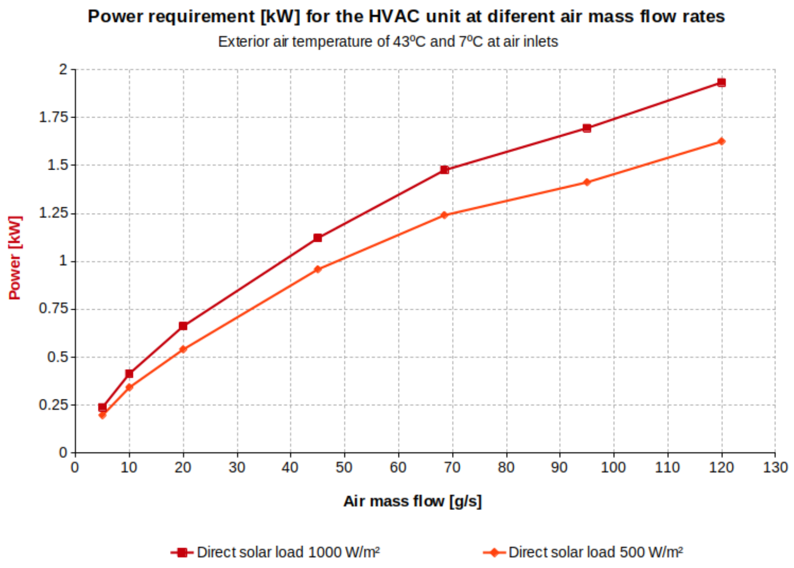

Figure 5.31: Power requirement [kW] for the HVAC unit at different solar loads

In the case of direct solar load 1000 W/m^2, it is required to reach an air mass flow rate of 120 g/s to reach optimal thermal comfort. It can be seen that the required power to cool down the car cabin at this air mass flow rate in a steady state is 1.93 kW, reaching an average air temperature of 23°C. In contrast, if the solar load is lower, at 500 W/m^2, only 95 g/s are required, which leads to a required power of 1.41 kW and an average air temperature of 21.8°C. A similar amount of power, 1.48 kW, is not enough to enter the thermal comfort range at 1000 W/m^2 solar load, corresponding to 68.5 g/s total air mass flow and 28.2°C of average temperature. The graphic below in Figure 5.32 shows the temperature at points of interest.

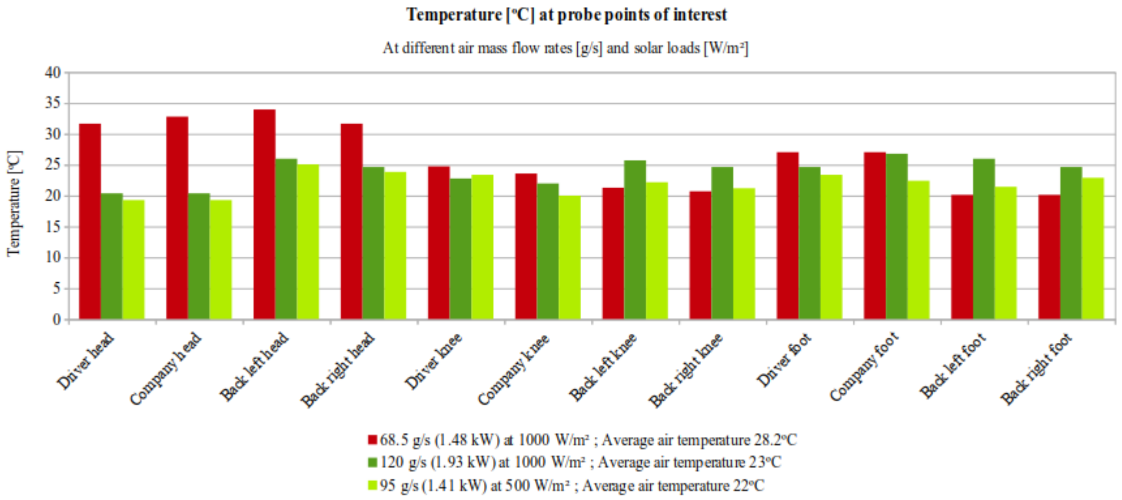

Figure 5.32: Temperature at point probes of interest

In Figure 5.33 it can be observed, for the 1000 W/m^2, how the CO_2 propagates inside the car cabin at different air mass flow rates. The visualised concentration of CO_2 is a threshold showing values between 725 and 40000 ppm. The concentration is higher at the side of the driver since it is the main source, while the right side is properly ventilated.

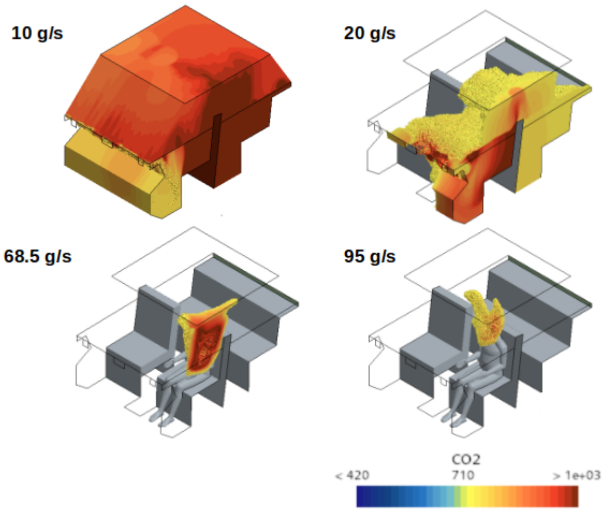

Figure 5.33: CO_2 concentration [ppm] at different air mass flow rates for a 1000 W/m^2 direct solar load

At 20 g/s it can be observed that there is a tendency to have higher carbon dioxide concentrations at lower average air cabin temperatures for low air mass flow rates. This is caused as a higher volume of warm air exhaled at high concentrations of carbon dioxide moves upwards in first place, to later continue to occupy the lower volume. For warmer cabin air scenarios, the exhaled concentrated air is not warm enough to move upwards and stays in lower zones until it is redirected outwards through the rear outlet (Figure 5.34). At least 15 g/s air mass flow rate is required to get proper levels of CO_2, reaching 725 ppm CO_2. From 45 g/s to higher air mass flow rates, the average concentration of CO_2 evolves similarly regardless the solar load.

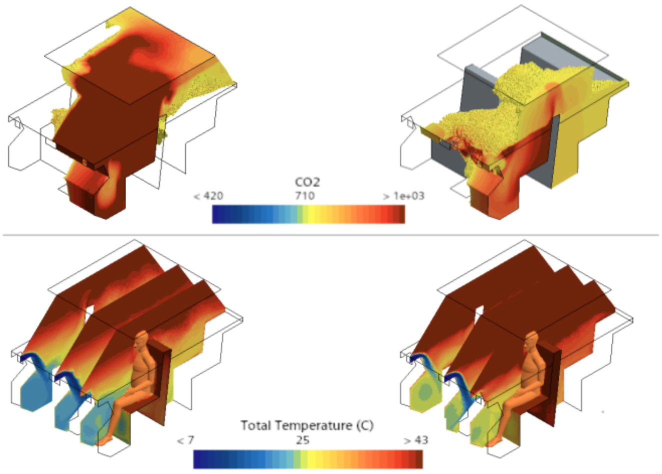

Figure 5.34: CO_2 concentration [ppm] and temperature [°C] at air mass flow rate 20 g/s for a 500 W/m^2 (left) and 1000 W/m^2 (right) direct solar load

5.1.10 Case 10: Transient analysis on air temperature and quality

Finally, in Case 10 transient simulations were carried out at air mass flow rates of interest. At 500 W/m^2, air mass flows at 10g/s and 68.5 g/s were studied.

For 10 g/s (Figure 5.35), it can be seen that in 15 minutes, the level of carbon dioxide concentration is approximately 960 ppm. This evolution is in accordance with the literature [1]. Therefore, reaching the poor air levels could around 20 minutes. In the case of the temperature, the steady state value of 40.9 °C is reached after 10 minutes of cooling.

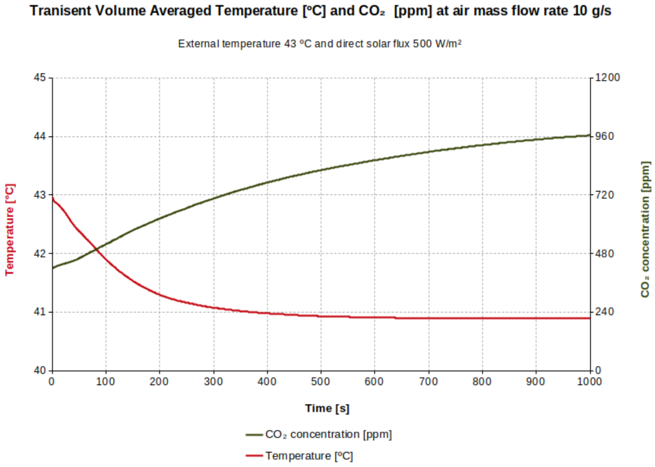

Figure 5.35: Volumetric average temperature [°C] and CO2 concentration [ppm] at 10 g/s and 500 W/m^2

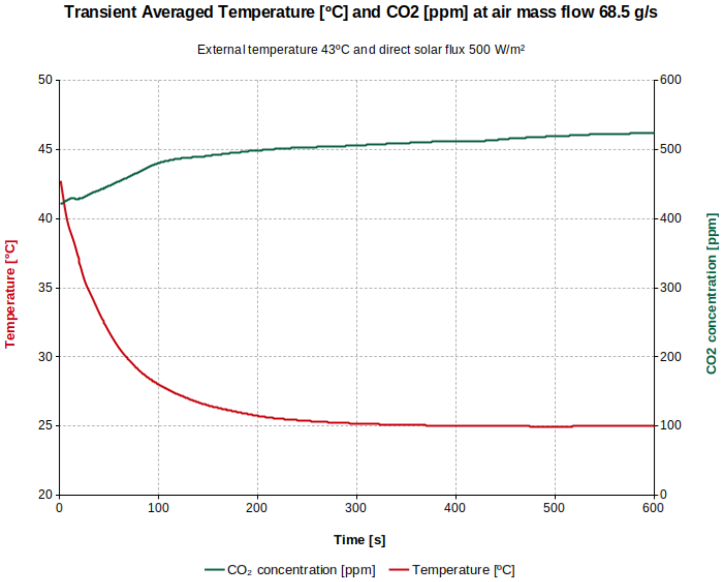

Figure 5.36: Volumetric average Temperature [°C] and CO2 concentration [ppm] at 68.5 g/s and 500 W/m^2

In the case of 68.5 g/s (Figure 5.36), only after 5 minutes the steady state in temperature of 25°C is attained. In the case of the concentration of carbon dioxide, the increase in time is slower. After 10 minutes the concentration of carbon dioxide is around 525 ppm while the steady state value should be around 540 ppm.

For 1000 W/m^2, the maximum air mass flow rate is studied (Figure 5.37). Only after 3 minutes the average volume temperature reaches the steady state with a value of 23 °C. In this case, as the ventilation is also high, the concentration of carbon dioxide also recahes the steady state, with a value of 460 ppm.

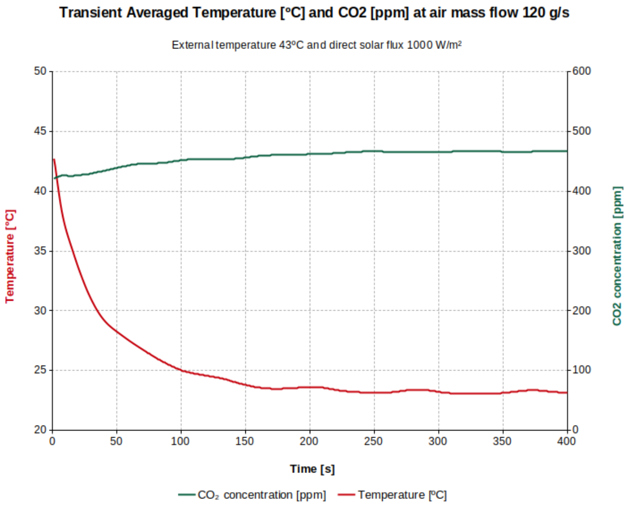

Figure 5.37: Volumetric average Temperature [°C] and CO2 concentration [ppm]

Overall, this transient study is useful to notice there is a requirement in air quality that must be met and it must be properly accounted for. Although the increase of CO_2 levels is slower with time if compared with temperature, it is still a determinant factor as traveling for more than 20 minutes is a usual scenario.

In the present study, regardless of the temperature within the car cabin, at least 15 g/s of ventilation is required to avoid drowsiness levels of carbon dioxide in the presence of a single passenger, which requires at least 0.4 kW of power from the HVAC unit. The increase in rate depending on the number of passengers could make this factor even more important, leading to higher necessary air mass flow rates to meet the requirement of air quality.

6

Conclusion

A thorough study has been carried out in order to explore the capabilities of CFD simulations in the context of BEV mobility. The main target for the present research was to study a cool-down scenario for warm conditions and set the requirements to achieve thermal comfort and air quality inside a simplified car cabin. Better understanding of the heat transfer effects in the cabin of a BEV can lead to a reduce in energy consumption a therefore to an improvement of the total driving range.

It has been observed that the solar loads in CFD simulations can not be ignored. It has been seen that variations in radiation from the solar loads have a stronger contribution to the warm temperature of the air inside the cabin if compared to the variation of levels of insulation at the car cabin boundaries.

It has also been shown that a specific amount of air mass flow rate at different air inlet distributions, can lead to different volume average air temperatures as well as to different local temperatures and heat fluxes through the cabin boundaries. Applying the full air mass flow rate to the top inlets instead of a fraction of it can lead to an increase of the average cabin air temperature and an increase of inwards heat through the windows as more cold air is directed towards the glass material.

At least 15 g/s air mass flow requires 0.4 kW to ventilate the car cabin to remain at 1000 ppm carbon dioxide concentration. It is recommended to remain below this level of carbon dioxide concentration to avoid drowsiness levels. Regarding thermal comfort, it has been quantified that in a summer day at 43°C is necessary to use at least 120 g/s and 1.9 kW HVAC power in the case of 1000 W/m^2 direct sun, achieving an average cabin temperature of 23°C. In contrast, it is only necessary to use at least 95 g/s and 1.41 kW HVAC power in the case of 500 W/m^2 direct sun, to reach an average cabin temperature of 21.8 °C.

Regarding transient simulations, a time-step of 1 second shows a good balance in accuracy and computational demand, useful to study the evolution of temperature and carbon dioxide levels within a car cabin. Air quality is a requirement to consider regardless of the temperature of the cabin, and of importance as the number of passengers increase.

To perform CFD simulations with a simplified car cabin seems to be a practical approach, reducing the computational requirements and easing the examination of the results. This approach enables the calculation of energy requirements for the HVAC units in BEV, which can imply a reduction in design costs for the development of BEV car cabins. Further research is required in order to accurately account for the thermal comfort of the passengers, as well as to understand the effects of drowsiness at high carbon dioxide levels in the car cabin models of study.

Bibliography

[1] Tong-Bou C., Jer-Jia S., Jhong-Wei H., Yu-Sheng L., Che-Cheng C., *Development of a CFD model for simulating vehicle cabin indoor air quality*, Transportation Research Part D: Transport and Environment Volume 62, July 2018, Pages 433-440.

[2] Rommelfanger C., Fischer L., Frisch J., and Van Treeck C., *Linearization of Thermal Equivalent Temperature Calculation for Fast Thermal Comfort Prediction*, Energies 2021, 14(18), 5922.

[3] Cvok I., Škugor B., Deur J., *Control trajectory optimisation and optimal control of an electric vehicle HVAC system for favourable efciency and thermal comfort*, Optimization and Engineering (2021) 22:83–102.

[4] Lee J.W., Jang E.Y., Lee S.H., Ryou H.S., Choi S., Kim Y., *Influence of the spectral solar radiation on the air flow and temperature distributions in a passenger compartment*, International Journal of Thermal Sciences Volume 75, January 2014, Pages 36-44.

[5] Tong Z., Liu H., *Modeling In-Vehicle VOCs Distribution from Cabin Interior Surfaces under Solar Radiation*, Sustainability 2020, 12(14), 5526.

[6] Torregrosa-Jaime B., Bjurling F. , Corber J.M., , Di Sciullo F., Paya J., *Transient thermal model of a vehicle's cabin validated under variable ambient conditions*, Applied Thermal Engineering Volume 75, 22 January 2015, Pages 45-53.

[7] Dancaa P., Bodea F., Nastase I., Meslemb A., *On the possibility of CFD modeling of the indoor environment in a vehicle*, Sustainable Solutions for Energy and Environment, EENVIRO 2016, 26-28 October 2016, Bucharest, Romania.

[8] Jonsson J., *Including Solar Load in CFD Analysis of Temperature Distribution in a Car Passenger Compartment*, (Master's Thesis) (2007), Luleå University of Technology, Sweden.

[9] Danca P., Bode F., Nastase I., Meslem A., *CFD simulation of a cabin thermal environment with and without human body – thermal comfort evaluation*, E3S Web of Conferences 32, 01018 (2018).

[10] Riachi Y., Clodic D., *A numerical model for simulating thermal comfort prediction in public transportation buses*, International Journal of Environmental Protection and Policy 2014; 2(1): 1-8.

[11] Dancaa P., Vartiresa A., Dogeanua A., *An overview of current methods for thermal comfort assessment in vehicle cabin*, Sustainable Solutions for Energy and Environment, EENVIRO - YRC 2015, 18-20 November 2015, Bucharest, Romania.

[12] Fojtlín M., Planka M., Fišer J., Pokorný J. and Jícha M., *Airflow Measurement of the Car HVAC Unit Using Hot-wire Anemometry*, The European Physical Journal Conferences 114:02023 (2016).

[13] Zhang H., Dai L., Xu G., Li Y., Chen W. and Tao W.Q., *Studies of air-flow and temperature fields inside a passenger compartment for improving thermal comfort and saving energy. Part I: Test/numerical model and validation*, Applied Thermal Engineering 29 (2009) 2022–2027.

[14] Zhang H., Dai L., Xu G., Li Y., Chen W. and Tao W.Q., *Studies of air-flow and temperature fields inside a passenger compartment for improving thermal comfort and saving energy. Part II: Simulation results and discussion*, Applied Thermal Engineering 29 (2009) 2028–2036.

[15] Versteeg H.K. and Malalasekera W., *An introduction to computational fluid dynamics: the finite volume method*, 2nd Edition Pearson Prentice Hall (2007).

[16] Ramesh Babu, A., Sebben, S., and Bark, T., *Effect of Cabin Insulation on the Heating Performance in EVs at Low Temperatures* SAE Technical Paper 2023-01-0763, 2023, https://doi.org/10.4271/2023-01-0763.

[17] Möller L., Sörensen L., *Thermodynamical Modeling of a Car Cabin* (Master's Thesis) (2011), Chalmers University of Technology, Göteborg, Sweden.

[18] Bredberg J., *On the Wall Boundary Condition for Turbulence Models* (2000), Chalmers University of Technology, Göteborg, Sweden.

[19] Shih T.H., Liou W.W., Shabbir A., Yang Z., and Zhu J. *A New k-ϵ Eddy-Viscosity Model for High Reynolds Number Turbulent Flows - Model Development and Validation* NASA Technical Memorandum 110446, 1995.

[20] Bryan R., Stewart E., Lightfoot N., *Transport Phenomena*, Second Edition, Chemical Engineering Department, University of Wisconsin-Madison.

[21] Incropera F., Denitt D., Bergman T., Lavine A., *Fundamentals of Heat and Mass Transfer.*

[22] Ferziger H., Peric M., *Computational Methods for Fluid Dynamics*, Third Edition.

[23] Kreith F., Boheman R.F., *Heat and mass transfer*, BocaRaton: CRC Press LLC, 1999.

[24] Rodi, W., *Experience with two-layer models combining the k-epsilon model with a one-equation model near the wall.* 29th AIAA Aerospace Sciences Meeting, 1991. 29.

[25] Wolfshtein, M., *The velocity and temperature distribution in one-dimensional flow with turbulence augmentation and pressure gradient.* International Journal of Heat and Mass Transfer, 1969. 12(3): p. 301-318.

[26] COMSOL, Multiphysics Cyclopedia.

[27] The Engineering ToolBox (2004). Air - Specific Heat vs. Temperature at Constant Pressure.

DEPARTMENT OF SOME SUBJECT OR TECHNOLOGY
CHALMERS UNIVERSITY OF TECHNOLOGY
Gothenburg, Sweden
www.chalmers.se

CHALMERS
UNIVERSITY OF TECHNOLOGY